

# FANCY MASTERARBEIT OF DEATH

Jonathan Förste

May 29, 2018



# CONTENTS

1	INTRODUCTION	5
2	PHYSICAL PROPERTIES OF TRANSITION METAL DICHALCOGENIDE MONOLAYERS	7
2.1	Crystal structure and symmetries . . . . .	7
2.2	Excitons in TMD monolayers . . . . .	8
2.3	Optical spectrum of wse <sub>2</sub> monolayers . . . . .	9
2.3.1	Phonon sidebands . . . . .	10
2.4	The valley zeeman effect . . . . .	11
2.5	Bilayer wse <sub>2</sub> . . . . .	13
3	PHYSICAL PROPERTIES OF TRANSITION METAL DICHALCOGENIDE MONOLAYERS	15
4	FABRICATION OF FIELD EFFECT STRUCTURES	17
4.1	Mechanical exfoliation . . . . .	17
4.1.1	Layer number . . . . .	18
4.2	Hexagonal boron nitride . . . . .	18
4.3	Electrode fabrication . . . . .	19
4.3.1	Top gate electrode . . . . .	19
4.3.2	Back gate electrodes . . . . .	21
4.4	Hot pick-up and transfer . . . . .	21
4.4.1	Annealing . . . . .	25
4.5	Electrical characterization . . . . .	25
5	SPECTROSCOPY OF WSe <sub>2</sub> GATE DEVICES	27
5.1	Optical setup . . . . .	27
5.2	Modelling peak shapes . . . . .	29
5.3	WSe <sub>2</sub> spectrum at different doping levels . . . . .	31
5.3.1	Photoluminescence spectrum . . . . .	31
5.3.2	Reflection spectrum . . . . .	33
5.4	Measuring the valley zeeman effect . . . . .	33
5.4.1	G-factors . . . . .	34
5.5	Comparison to bilayer wse <sub>2</sub> . . . . .	36
6	SUMMARY & OUTLOOK	39



# 1 INTRODUCTION

Ever since Andre Geim and Konstantin Novoselov were awarded the Nobel prize for their discovery of graphene, two-dimensional materials have become a centerpiece of condensed matter physics. After graphene, a lot of 2D materials were found, including transition metal dichalcogenides (TMDS). These 2D-semiconductors have attracted a lot of attention recently because of their unique valley physics, incorporating a pseudo-spin-like degree of freedom, that can be optically addressed([referenzen](#)). This has created a hype around TMD monolayers, that led to important milestones in the new field of “valleytronics”, notably the valley hall effect[1] and the coherent manipulation of excitons with femto-second light pulses[2]. But TMD monolayers have gained attention not only because of their potential applications, but because the nature of these materials offers a unique model system to study physics in two dimensions. On the optics side, this is mainly due to the special properties of optically excited excitons in TMD monolayers. The confinement to two dimensions enables exciton formation well above room temperature and offers interesting applications as well as a system to study few- and many-body physics. Point defects can lead to formation of quantum dots, that have shown characteristics of single-photon emitters. The high absorption efficiency of their direct bandgap enables strong coupling and the creation of exciton polaritons, bosonic superpositions of excitons and photons.

However, the research into these materials is still young, and the physical processes governing their light-matter interaction are not completely understood. The optical spectrum of TMDS still shows a lot of unknown features, that need to be identified to get a good understanding of the involved physics and to pave the way for future applications.

While the spectrum is governed by the formation and recombination of excitons, especially tungsten-based TMDS show a rich ensemble of different peaks. The focus of this thesis lies primarily on the material  $\text{WSe}_2$ . Its unique band structure puts it between direct and indirect semiconductors and shows signatures of both types. Direct excitons and charged trions as well as momentum-indirect excitons, that decay via phonon sidebands. Indirect excitons offer a wide-ranging model to explain the complex spectrum of  $\text{WSe}_2$ . Yet the research on TMDS is still limited by sample quality.

Spectral features can vary greatly from sample to sample, that can exhibit different levels of intrinsic unintentional doping, strain and contamination from the fabrication process. Meaningful spectroscopic studies are therefore tethered to the fabrication of high quality monolayers, that show a “pure” spectrum, including spectral lines that show little inhomogenous broadening, no defect driven features and are compensated for unintentional doping. A big step towards this goal can be achieved by suspending TMDS in hexagonal boron nitride, that offers an optimal dielectric environment to observe spectral lines, close to the homogenous linewidth. To compensate for intrinsic doping, samples have to be gate tuned with an applied voltage.

## *1 Introduction*

The goal of this thesis was to establish a pipeline to fabricate samples in this manner. This process utilizes the well established method of mechanical exfoliation for the production of TMD monolayer samples and hBN substrate and capping layer. Using the novel fabrication technique of “hot pick-up and stamping” hBN-TMD heterostructures are built and contacted to gold structures, that are fabricated with contact lithography. Photoluminescence and differential reflection measurements demonstrate the increased quality and gate-tunability.

The thesis is divided into three sections. The first part summarizes the physical properties of TMDS that are relevant for optical studies. Then the fabrication and characterization of hBN-encapsulated samples is described in detail followed by experimental analysis of the reflection and photoluminescence spectrum of  $\text{WSe}_2$  monolayers for different charge densities and magnetic fields.

## 2 PHYSICAL PROPERTIES OF TRANSITION METAL DICHALCOGENIDE MONOLAYERS

### 2.1 CRYSTAL STRUCTURE AND SYMMETRIES

Transition metal dichalcogenides (TMDS) belong to a class of materials that consist of large covalently bound sheets, that are held together by weak van-der-Waals forces. These so-called layered materials are known for their most famous member graphene. While graphenes band structure with its characteristic dirac cones gives it exceptional electronic properties, the lack of a band gap led to the investigation of other layered materials. TMDS have long been known as indirect band gap semiconductors but only since the discovery of graphene their properties in the limit of one atomic sheet—the monolayer—came into focus. Crystals of TMDS, as their name suggests, consist of a tri-atomic base of one transition metal atom like tungsten (w) or molybdenum (Mo) and two chalcogen atoms like sulfur (s), selenium (se) or tellurium (t). When these compounds are arranged laterally, they form a TMD monolayer (see figure 2.1 A). TMDS can exist in different metastable phases, that have a different crystal structure as well as different electronic properties[5]. The stable semiconducting phase is called 2H. In this configuration every transition-metal atom has six neighboring chalcogen atoms and forms a trigonal prismatic unit-cell, with the transition-metal in the center as depicted in figure 2.1 B. A TMD monolayer exhibits a  $D_{3h}^1$ -symmetry. The unit-cell is invariant under 3-fold rotation as well as in-plane reflection. In the top-view (see figure 2.1 C) this looks similar to the hexagonal lattice structure of graphene, but with the key difference of a broken inversion symmetry. When the unit-cell is inverted with the transition metal atom as its inversion center, the chalcogen atoms wind up in empty locations as with any possible inversion point.

This has two important consequences, regarding the electronic band structure. As in graphene, the reciprocal lattice is hexagonal. At the K points however, instead of the characteristic dirac cone, TMDS form a direct band gap in the monolayer limit. Whats more, because of inversion symmetry breaking the degeneracy of the K points is broken into the two distinguishable K and K' points that are identical in graphene. This leads to special optical selection rules coupling the different valleys to light with opposite helicity, leading to a new optically controllable and detectable degree of freedom—the valley-index. Analogous to electronics and spintronics, the term “valleytronics” has been coined to describe possible information processing by manipulating this property[3, 4]. The band structure in the vicinity of the K valley is mostly dominated by the *d*-orbitals of the heavy transition metal atoms and exhibits strong spin-orbit coupling. In the valence band, this leads to a splitting of around 160 meV for opposite spin. This energy is large enough to suppress any transition between the two valence subbands even at room temperature. Because of time-reversal symmetry, the splitting is reversed in the K' valley. In an optical transition this means, that valley and spin are tightly locked.

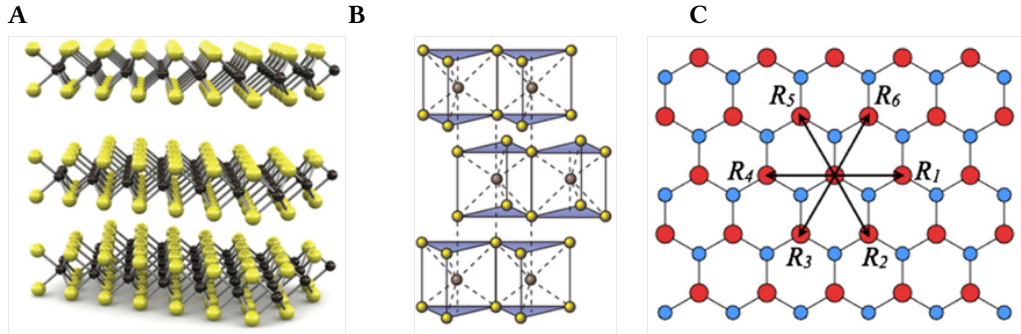


Figure 2.1: Crystal structure of TMDS: **A** TMDS are composed of large sheets of transition metal atoms sandwiched in between chalcogenide atoms. The covalent bonds strongly hold the layers together in-plane, while the individual sheets are only weakly bound by van-der-Waals forces. **B** In the 2H phase, the unit cell of TMDS has a triagonal prismatic shape with the transition metal in the center, between two triangles of chalcogenide atoms. **C** Viewed from the top, TMDS show a hexagonal lattice structure. However, because of the structure of the unit cell, the inversion symmetry is broken. Graphics from[3, 4]

## 2.2 EXCITONS IN TMD MONOLAYERS

When an electron absorbs a photon of an energy higher than the band gap of a semiconductor, it gains enough energy to be elevated to the conduction band and can thus move freely through the crystal. Other electrons can hop to the vacancy making this hole just as free as the excited electron. It also effectively acts like a positive charge, which means that there are Coulomb forces between the free electron and the hole. When this interaction is strong enough to overcome thermal excitations, the two quasiparticles can enter a bound state, called “exciton”. In a bulk semiconductor electrons in between electron and hole weaken this interaction and thus result in a low exciton binding energy. The direct semiconductor GaAs for example exhibits an exciton binding energy of just 4.2 meV. Doing a rough calculation with  $T = E_{binding}/k_B$  this corresponds to a temperature of 48 K limiting exciton formation to samples cooled well below the temperature of liquid nitrogen. The geometry of TMD monolayers however effectively reduces the screening effect. Because the movement of electrons and holes is confined to two dimensions, the electric field density in the material drops significantly and the strong Coulomb interaction between the free quasiparticles raises the exciton binding energy to about 500 meV[6], roughly corresponding to nearly 6000 K. Therefore excitons can be excited at room temperature. Their strong interaction results in an exciton Bohr radius of close to 1 nm and a very short lifetime in the order of picoseconds. Hence, the recombination of excitons with emission of a photon is the most efficient optical decay channel and thus dominates the photoluminescence spectrum. The decay also happens much faster than the so called valley lifetime—the timescale of coupling between the valleys—preserving the helicity in their emission once they decay. This is called “valley polarization”. The thinness of TMD monolayers

### 2.3 Optical spectrum of wse<sub>2</sub> monolayers

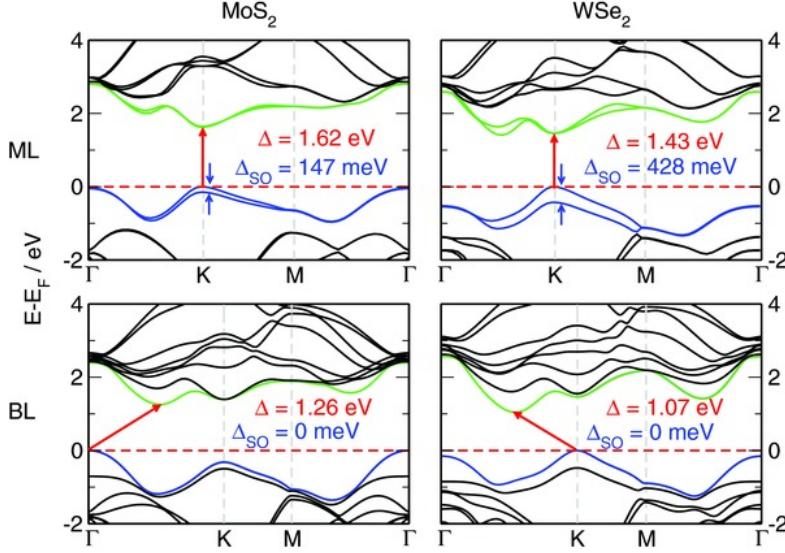


Figure 2.2: Band structure for MoS<sub>2</sub> and WSe<sub>2</sub> mono- and bilayers calculated for room temperature. In the limit of a single atomic layer TMDS form a direct band gap at the K-point and the valence band is strongly split due to spin-orbit coupling. Graphic taken from [14].

has additional implications. Because the electric dipole field of the exciton extends beyond the boundaries of the crystal, the dielectric environment has a big influence on the optical spectrum[7–9]. Impurities such as microscopic water droplets or dangling bonds of silicon oxide can induce localized potentials, broadening the linewidth of the PL features, thus complicating spectroscopic studies. On the other hand, this high sensitivity could be used in quantum sensing applications to optically probe or visualize electric or magnetic proximity effects[10–13].

## 2.3 OPTICAL SPECTRUM OF WSe<sub>2</sub> MONOLAYERS

The optical spectrum of TMDS both in reflection and PL is dominated by excitonic effects. In WSe<sub>2</sub> especially the PL spectrum shows a rich ensemble of characteristic spectral features, that so far have not been identified completely and the discussion around the underlying processes is still active.

For hBN encapsulated WSe<sub>2</sub> the main exciton resonance (X) is located at around 1.72 eV. This resonance corresponds to the creation and annihilation of an exciton in the K valley with electron and hole having a parallel spin component ( $X_l$ ). The corresponding exciton with antiparallel spins is often called the dark state as its “spin-forbidden” ( $D/X_u$ ). Its radiative decay is only allowed in-plane, because of symmetry reasons™. Because of spin-orbit coupling this state lies about 40 meV lower than the bright exciton[16]. The PL from these excitons can be collected from the side or with a high numeric aperture objective, that catches light not directly emitted in the z-direction[17, 18]. In the presence of free charges, either holes or electrons, exci-

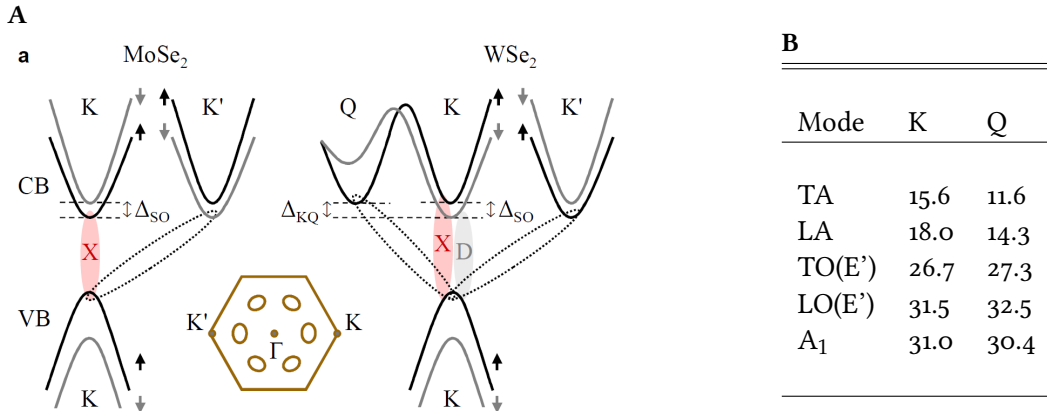


Figure 2.3: **A** Diagram of the band structure of MoSe<sub>2</sub> and WSe<sub>2</sub>. The spin-like bright transition (X) in WSe<sub>2</sub> does not have the lowest energy. Because of spin-orbit coupling, the K valley with opposite spin is lower in energy, as well as the spin-like but momentum indirect K' and the Q-valley. This results in a multitude of possible optical transitions. **B** Phonon energies in meV for all modes that can couple to charge carriers and have the right momentum to form a sideband[15].

tons can interact with them to form trions that are associated with a redshift of 20–30 meV[19]. While these properties can be predicted by modeling the trion as a three-body quasi particle, its precise nature still remains under discussion. The most contrarian interpretation to the helium-like bound state is a so-called fermi polaron. In a charged regime excitons behave like an impurity in a “sea” of electrons, forming the polaron quasi particle[20–22].

The spectrum of WSe<sub>2</sub> shows additional features, have so far escaped thorough understanding. In light of strong sample-to-sample variation, they are commonly attributed to localized effects, like defect-induced quantum dots or local doping[23, 24], that create trapped excitons. Improved fabrication techniques like mechanical exfoliation and the usage of hBN as a substrate (see section 4) have enabled experimentalists to measure spectra with very little defects and narrow linewidths, that still show a rich class of features, that are reproducible in other samples as well as in the samples used in this work.

### 2.3.1 PHONON SIDEBANDS

Our group recently proposed a model identifying these peaks as phonon side-bands of momentum-indirect excitons[25]. It has recently been shown, that in contrast to molybdenum-based TMDS WSe<sub>2</sub> actually shows an indirect band gap[26, 27]. As can be seen in figure 2.3 A, the Q-valley lies energetically close to the K-valley and is suggested to be lower than the upper K-valley, that participates in the direct spin-like exciton transition. This could point to a high population of excitons composed of electrons in Q as well as in the lower lying spin-like K'-valley. While both these states are spin-allowed, momentum conservation prevents them from radiatively decaying in a single-photon process. Instead they can recombine with assistance of an additional phonon, carrying the inter-valley momentum. For momentum conservation to hold the

following equations has to be fulfilled for momentum-indirect excitons in  $Q$  or  $K'$  respectively:

$$\vec{k}_K + (\vec{k}_K - \vec{k}_{Q/K'}) = \vec{k}_K + \vec{k}_\gamma + \vec{k}_{phonon} \quad (2.1)$$

$$\Rightarrow \vec{k}_{phonon} \stackrel{!}{=} \vec{k}_K - \vec{k}_{Q/K'} \quad (2.2)$$

Because of the hexagonal structure of the Brilloin zone  $\vec{k}_K - \vec{k}_{K'}$  simply equals a phonon in  $K$  whilst  $\vec{k}_K - \vec{k}_Q$  is conveniently close to a phonon in  $Q$ . Crystal vibrations in TMDS can have three acoustic and six optical modes, but only two acoustic and three optical modes can couple to charge carriers. This leaves a total of five possible phonon sidebands for both  $Q$ - and  $K'$ -indirect excitons, neglecting processes involving more than one phonon. Corresponding, theoretically calculated energies can be found in 2.3 B[15]. The phonon replica would appear as a peak redshifted by these energy values. For  $K'$ -indirect excitons the positions of the peaks can be inferred directly, since the energy splitting between the spin-like and spin-unlike exciton is known and both features can be measured. The  $Q$ -valley however has no direct decay channel. Its energy thus has to be fixed inductively, by looking for peaks that fit the pattern, given by the phonon energies and calculate backwards.

[28]

## 2.4 THE VALLEY ZEEMAN EFFECT

A splitting of spectral lines in presence of a magnetic field has been studied for over a hundred years and is called the Zeeman effect, named after the scientist first measuring it in the spectral lines of sodium. The shift of different energy levels in an atom results from the magnetic moment of the state, caused by its orbital angular momentum and spin. Solid crystals are essentially large ensembles of atoms that merge atomic orbitals to form the electronic band structure, that can shift in a magnetic field just as orbitals of single atoms. The 2D-nature of TMD monolayers and their broken degeneracy of the  $K$  and  $K'$  point gives rise to a meta-phenomenon called the “valley Zeeman effect”, that leads to a shift in the band gap energy that is different for both valleys, leading to a split of spectral lines with different circular polarization[29, 30]. In the vicinity of the  $K$  point the band structure is dominated by the large  $d$ -orbitals of the transition metal atoms. The hybridized  $d_{x^2-y^2} \pm id_{xy}$  orbitals give the valence band an orbital angular momentum along  $z$  of  $l_z = 2\hbar$  that leads to a magnetic dipole moment of  $\mu_{K,orb} = 2\mu_B$ . The conduction band is primarily formed by the  $d_{z^2}$ -orbital that has no out-of-plane angular momentum and therefore no magnetic moment along  $z$ . This leads to an asymmetric shift in the conduction and valence band and therefore to a shift of the band gap energy. The TMD-geometry confines electron movement to the 2D plane, forcing the magnetic moment to either point upwards or downwards out of plane. This direction is exactly opposite at the  $K$  and  $K'$  points, shifting the valence band energy, and thus the band-gap in opposite directions. The total orbital magnetic moment at  $K$  has a value of  $\mu_{K,orb} = 2\mu_B$ . For the bright spin-like exciton transition this leads to a valley splitting of  $\Delta_{K,K'} = 4\mu_B B_z$ . The prefactor in this equation is often called the  $g$ -factor and is given in units of the Bohr magneton  $\mu_B = e\hbar/2m_e$ . As it turns out, this first simple result is already in good agreement with experimental studies (see

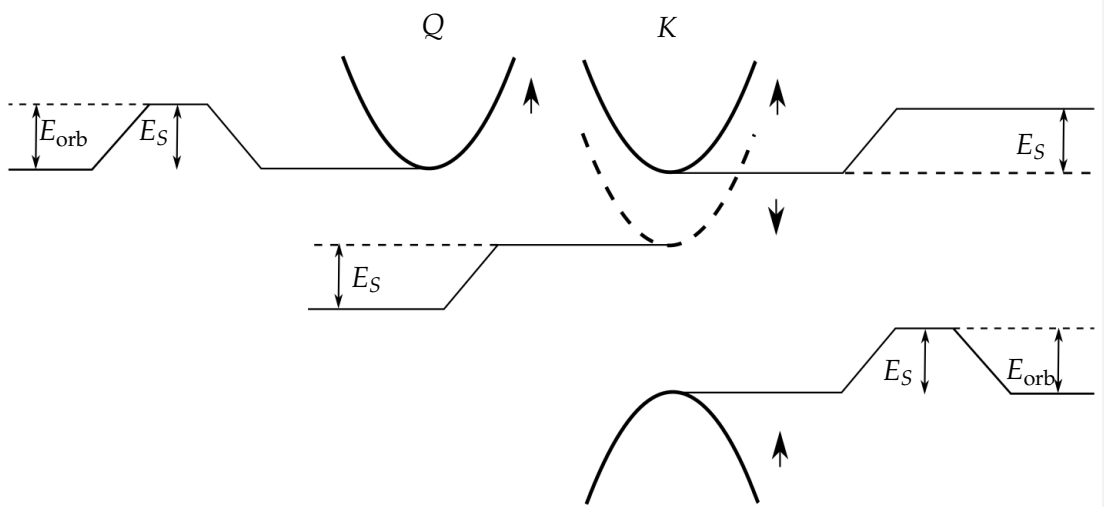


Figure 2.4: Diagram of orbital and spin contributions to the valley Zeeman effect. For excitons with parallel spin, the corresponding shift  $E_S$  of conduction and valence band cancels out. The shift for the direct spin-like exciton therefore depends mostly on the magnetic shift of the orbitals  $E_{\text{orb}}$  that at the  $K$  point is non-vanishing only in the valence band. The spin-unlike direct exciton however has a strong spin contribution which in theory doubles its  $g$ -factor. For momentum-indirect excitons in  $Q$  the  $g$ -factor almost entirely due to the difference in effective mass between hole and electron, because both  $E_S$  and  $E_{\text{orb}}$  shift in the same direction in the conduction and valence band.

chapter 5) but this is only because for this particular state, other contributions are small or cancel each other out. The main additional contributions are the spin of electron and hole and their respective effective masses. This leads to the following formula:

$$\Delta_B = g\mu_B B_z = 2\mu_B B_z \left[ (\tau_{e,\text{orb}} - \tau_{h,\text{orb}}) + g_e(S_e - S_h) + \left( \tau_e \frac{m_0}{m_e} - \tau_h \frac{m_0}{m_h} \right) \right] \quad (2.3)$$

The first part of this equation belongs to the angular momentum of the orbitals forming the band structure. In the conduction band this value is  $\tau_{e,\text{orb}} = \pm 2$  for  $Q/Q'$  while it vanishes for  $K/K'$ . Only the  $K/K'$  valleys are involved in the valence band and as discussed, their contribution is  $\tau_{h,\text{orb}} = \pm 2$ . The second term in (2.3) corresponds to the spin component of electron and hole. The spin of each particle has a value of  $S = \pm 1/2$  which is multiplied by the single-electron  $g$ -factor of  $g_e = 2$ . The last term represents the correction from the quasi-particle effective masses with  $\tau_{e/h} = \pm 1$  representing the opposite direction of the magnetic moment in  $K/K'$  or  $Q/Q'$ .

In the spin-like direct exciton  $X$ , the observed  $g$ -factor of  $g_X = 4$  mostly stems from the orbital angular momentum with parallel spin components canceling each other and a small

difference in the effective mass term in the same valley. For the spin-unlike exciton  $D$ —all else being equal—the spins of electron and hole point in opposite directions. Neglecting the mass term this yields a  $g$ -factor of  $g_D = 8$ . Predicting the  $g$ -factor for momentum-indirect excitons is more challenging though, because the difference in effective mass plays a more important role when electron and hole are coming from different valleys. Calculating the effective mass at a point point in  $k$ -space can be done using a variety of theoretical approaches as done for example in [31] for the  $K$ -valley.

## 2.5 BILAYER WSE<sub>2</sub>

Even a second layer fundamentally changes the properties of wse<sub>2</sub>. Inversion symmetry is no longer broken and the  $Q$  valley drops below  $K$  in energy, yielding an indirect band gap[14]. At zero electric and magnetic field there is also no spin-orbit coupling and valley polarization. However, a gate voltage can reinstate this property and could be used as a switch in a potential device[32] What is also interesting about bilayer wse<sub>2</sub> in particular is, that spin and valley degree of freedom are also coupled to the layer pseudospin, the location of the excited electron in one of the two layers of the sample[33].

While the  $K$  valley in the valence band is still at the highest energy, the  $\Gamma$  valley is located only 30-40 meV below. This means that the majority of PL of wse<sub>2</sub> bilayers originates from the decay of momentum-indirect excitons with electrons in  $Q$  and holes in  $K$  or  $\Gamma$ . PL from excitons involving electrons in  $K$  such as the direct bright and dark exciton should yield much less intensity.



### **3 PHYSICAL PROPERTIES OF TRANSISION METAL DICHALCOGENIDE MONOLAYERS**



## 4 FABRICATION OF FIELD EFFECT STRUCTURES

The main goal of this thesis was to implement a fabrication pipeline for TMD monolayer samples, that yields narrow linewidth optical spectra and gate-tunability, enabling more accurate spectroscopic studies. This process builds on the work presented in [34]. Using the same mechanical exfoliation process in combination with standard micro lithography techniques and an advanced stamping procedure, this yields a fast and increasingly reliable process to build charge-tunable heterostructures of various 2D-materials.

### 4.1 MECHANICAL EXFOLIATION

Thin films of TMDS, like many natomaterials, can be fabricated using a top-down or bottom-up approach. Bottom-up these materials can be grown via chemical-vapor deposition (CVD)[35]. Because of its scalability it is the leading candidate for an industrial fabrication pipeline. However, the top-down approach of mechanical exfoliation has become the first choice for a lot of projects to build high quality model systems, that can be used to study physics in low dimensions[36]. The reason is the so far superior quality of few-layer flakes in terms of defects and contaminants as well as the synergy with dry transfer methods(See section 4.4).

The mechanical exfoliation process—often referred to as the “scotch tape method”—is based on the fact, that the van-der-Waals forces between adjacent layers in TMD’s are much weaker, than the lateral covalent bonds—weak enough, that they can be easily broken apart by adhesive tape. The starting point is a solid crystal of TMD-material, that can be produced either naturally or synthetically with high purity (supplied by hq-graphene). When a stripe of adhesive tape is brought in contact with it, a small amount can be peeled off. With a second stripe, that is put on the first one, the process is repeated multiple times. Each time, the fresh tape is peeled off its parent, the strong adhesion between tape and TMD ensures a clean interface. Three to four repetitions are an optimum to produce monolayers of a useful size. More repetitions further thin the material but heighten the risk of these thin films to break to smaller pieces, which complicates processing the flakes later on and build larger devices.

To prepare monolayer flakes for the assembly of more complex devices, they first have to be transferred onto a suitable substrate. In this work, this substrate is silicon with a layer of thermal oxide that is between 50 and 90 nm thick. Before wafers of this material are brought in contact with the exfoliation tapes they are cleaned both in acetone and isopropanole before being exposed to oxygen plasma for 180 s. This ensures a clean surface and maximizes the material that sticks to the wafer([37]). To release the tape the substrate is heated to 85°C for at least 2 minutes. After cooling down the tape can be peeled off and the wafer is inspected for monolayers. As seen in 4.1, this process yields a large number of flakes of different sizes and thicknesses on the substrate and it is common not to find a suitable monolayer sample on a typical si-substrate (10 mm by 10 mm).

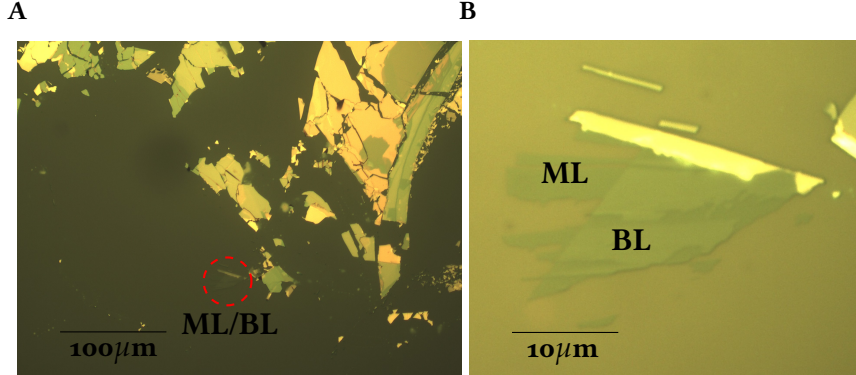


Figure 4.1: **A** During the exfoliation process a lot of flakes of different size and thickness are scattered over the substrate. Interesting specimen have to be searched for by hand. **B** Flake consting of mono- and bilayer regions that can be identified by their optical contrast.

#### 4.1.1 LAYER NUMBER

Under an optical microscope (Olympus® - BH2-UAMA)monolayers can be identified using optical contrast and color as features to distinguish them from thicker films. It is possible to verify the layer number by this criteria alone using a camera and image analysis software[34]. However, this is much more reliable on transparent substrates, since the optical contrast is higher with an out-of-focus dark background. A reflective surface however enhances inhomogenities in the lighting conditions, making it harder to rely on absolute values of intensity. With our optical microscope and si/sio<sub>2</sub> substrates, monolayer candidates where instead verified using photoluminescence (PL) imaging[13]. In TMDS only monolayers show a direct band gap. Therefore even bilayers are much less efficient photonic emitters, showing almost an order of magnitude less PL -intensity. The sample is excited with a laser with a wavelength above the direct exciton resonance and only the PL is collected on the chip of a USB-camera. A detailed description of the optical setup can be found in 5.1. An sample measurement, comparing mono- and bilayer regions of wse<sub>2</sub> in a standard microscope image with PL -imaging can be seen in figure 4.2.

Other methods to idetify monolayers inlcude both PL and Raman spectroscopy[38–40]. However, to fit in a fast assembly pipeline PL-imaging proved to be the best method to verify the layer number as well the overall quality of the sample.

## 4.2 HEXAGONAL BORON NITRIDE

For spectroscopic studies of TMD's the right substrate plays a very crucial part. As discussed in section 2.2, the ultra-thin geometry of TMD monolayers makes them very sensitive to the dielectric environment. To obtain a narrow linewidth of the spectral features both in reflection and PL spectroscopy, a suitable substrate has to fulfill some important specifications. A minimal surface roughness—ideally be atomically flat—avoids local modulation of the band structure

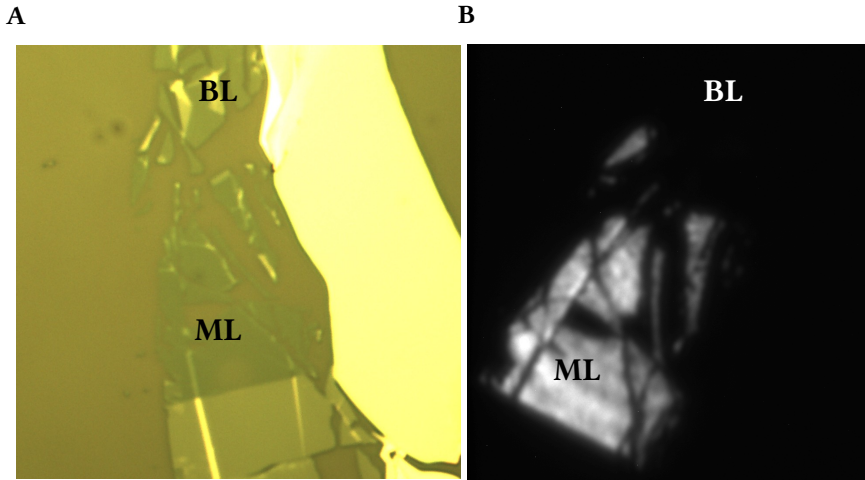


Figure 4.2: Comparison of mono- and bilayers of  $\text{WSe}_2$ . **A** The reflectance contrast of mono- and bilayers can be used to measure the layer number. The difference is however small enough to misidentify them under changing or inhomogeneous lighting conditions. **B** The PL -intensity of the monolayer is almost an order of magnitude higher than the bilayer and can therefore be identified very easily.

through strain. Also, the substrate has to be dielectrically calm to avoid local doping effects, that just like strain can introduce localized potentials, that broaden the linewidth. Both criteria rule out traditional substrates such as  $\text{Si}$  and  $\text{SiO}_2$ . In recent years hexagonal boron nitride (hBN) has proven to be the superior choice to observe narrow linewidth spectra in TMD's[41]. HBN, just like TMDS is a layered material, but belongs to the class of 2D-isolators, with a large, indirect band gap in the UV-range[42]. Thin, flat layers of hBN can be mechanically exfoliated and achieve large, flat terraces. Few layers are sufficient to shield a TMD sample from the underlying substrate. To achieve even narrower lines, it can be "sandwiched" between two flakes of flat hBN as was done with all samples contributing to this thesis. From the standpoint of nanofabrication hBN has another important property. The van-der-Waals forces at hBN-TMD interfaces are stronger than between TMDS and  $\text{SiO}_2$ . This is an important requirement for the hot pick-up assembly, discussed in section 4.4.

### 4.3 ELECTRODE FABRICATION

A gate-tunable TMD-device can be understood as simple capacitor. A gate voltage is applied between the TMD-flake and the doped Si substrate—separated by a 50 nm layer of thermal  $\text{SiO}_2$ .

#### 4.3.1 TOP GATE ELECTRODE

To contact microscopic structures like TMD-monolayers, electrodes have to be fabricated using micro-lithography. TMD monolayers—either CVD-grown or exfoliated—are scattered on their

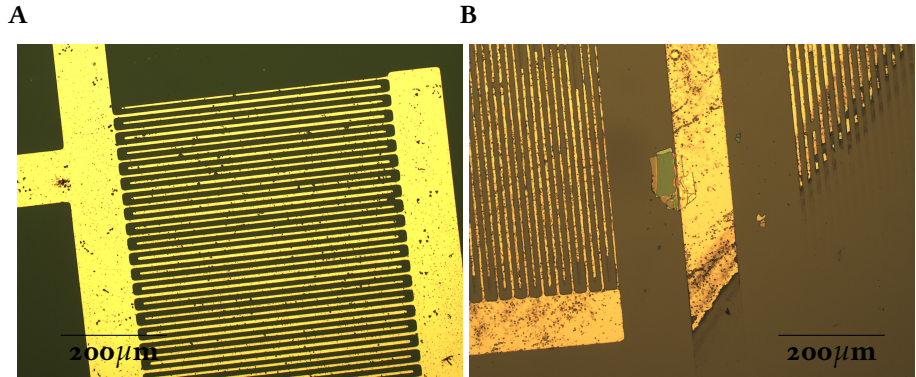


Figure 4.3: **A** Electrodes are written onto the substrate prior to the assembly of the hBN-TMD heterostructure. A preused chromium mask of an interdigital structure is used for the gold pattern. **B** As long the heterostructure is dropped in contact with a thick line of the gold pattern, minor defects in the electrode structure do not affect the functionality of the device.

substrates randomly. Therefore it is a common practice to fabricate electrodes directly on top of the sample via e-beam or laser lithography(Referenzen). Samples encapsulated in hBN usually feature one or more additional films of graphene that provide an ohmic contact outside the heterostructure. Since only one contact is sufficient for charge-tunability, the process can be simplified greatly. Instead of writing electrodes after transfer, contacts are fabricated on the bare substrate. The encapsulated hBN-TMD-heterostructure can be contacted by dropping it on the edge of the gold structure. Most of the time, more TMD-material than the monolayer is picked up during the transfer process. Because a TMD-gold interface is conducting even at very low temperatures, these flakes provide suitable contacts, that do not have to be encapsulated in hBN, therefore replacing additional graphene electrodes. Gold patterns are fabricated in contact lithography using a chromium mask that is deposited on glass. Because the stack can be dropped at any point on the substrate, the shape of the gold structure is unimportant, as long as it is large and connected. Therefore not even a new lithographic mask had to be fabricated. Instead a suitable mask was chosen from old pre-used structures. Even defects and deterioration of the masks only manifests aesthetically, rendering this process very robust and ideal for batch fabrication of gate-structures. The recipe starts with spin coating positive AZ 701 photoresist on a Si/SiO<sub>2</sub> wafer. Using a maskaligner, the wafer is brought in contact with the chromium mask before exposing it to uv-light for 18 seconds. After that, the pattern is developed using AZ 826 MIF developer, that washes out the exposed photoresist.

In the next step, the sample is coated in an X-ray evaporation system. First, a 1-5nm film of titanium is deposited on the substrate, that acts as a bonding agent. Subsequently a 50nm film of gold is deposited on top. After removing the sample from the vacuum chamber, the structures are finished in the so called “lift-off”. The substrate is simply suspended in a solvent like acetone, that dissolves residual photoresist, only leaving gold, deposited in the developed. To speed up the lift-off process, the sample can be placed in an ultrasonic cleaner at a low

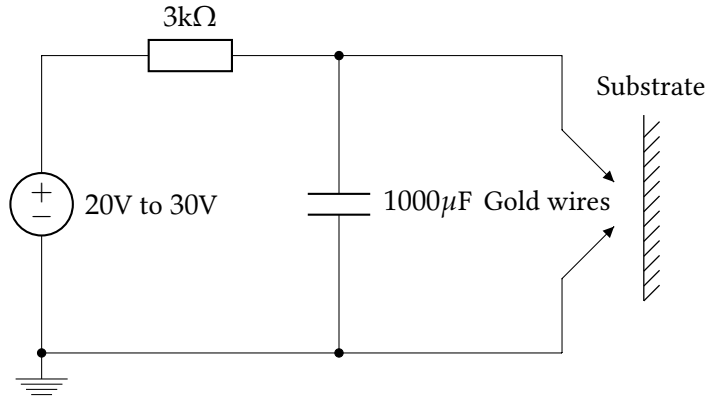


Figure 4.4: Circuit diagram for back gate fabrication: A capacitor is charged at 20V to 30V.

Two boron-doped gold wires are moved very closely to the silicon substrates. Once the distance between the wires and the substrate is low enough, an electric arc forms, discharging the capacitor through the substrate. Heat from the high current melts the tip of the gold wire locally doping the silicon and creating a gradient semiconductor/metal-interface.

power. The resulting structure can be seen in figure 4.3.

#### 4.3.2 BACK GATE ELECTRODES

Silicon is a semiconductor. A simple contact with a metal wire therefore results in a Schottky barrier at low temperatures. To create an ohmic contact to the backgate, the semiconductor/metal interface is “smeared out” by diffusing boron doped gold into the substrate (see figure 4.4). This is achieved by applying a high voltage between two gold wires and bringing them close to the substrate. Because the Si-substrate has a higher conductivity than the ambient air, an arc discharge between the tips of the wires will preferably find its way through the substrate. When the arc forms the tips of the gold wire evaporate and penetrate the Si-substrate. This creates a gradual metal-semiconductor interface and avoids a Schottky barrier, leaving a small gold droplet on the surface that can be contacted to a thin wire using conducting paste.

This process can be very violent. Gold droplets can splash over a large distance and evaporated gold can not only diffuse into the backgate but can also contaminate the  $\text{SiO}_2$  surface, lowering the breakdown voltage significantly. Therefore this step in the fabrication process should be taken before assembling the TMD-hBN heterostructure. This way, the substrate can be replaced in case of failure.

## 4.4 HOT PICK-UP AND TRANSFER

The mechanical exfoliation method is popular also for its synergy with dry transfer methods. CVD-grown TMD-flakes are grown on suitable substrates and can be transferred to a target substrate using a variation of wet methods, that involve powerful solvents or a combination of

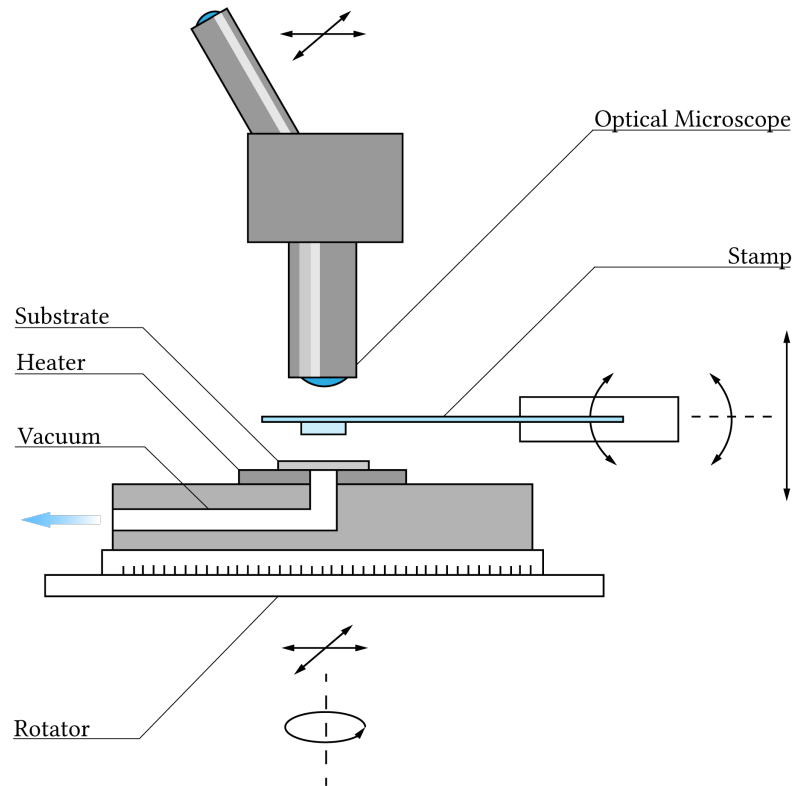


Figure 4.5: Setup for hot pick-up and stamping. The substrate is placed on a small, round **ceramic heater** with a 3mm hole in the center(Referenz Thorlabs), that is PID-controlled and can reach temperatures up to 200°C. It is mounted airtight onto the massive sample holder, that is connected to a **vacuum pump** to hold the **substrate** in place. It is **fully rotatable** and can be moved in plane. The PDMS/PPC **stamp** is mounted to a z-translator and can be tilted with respect to both in-plane axes. The **optical microscope** can also be moved in-plane.

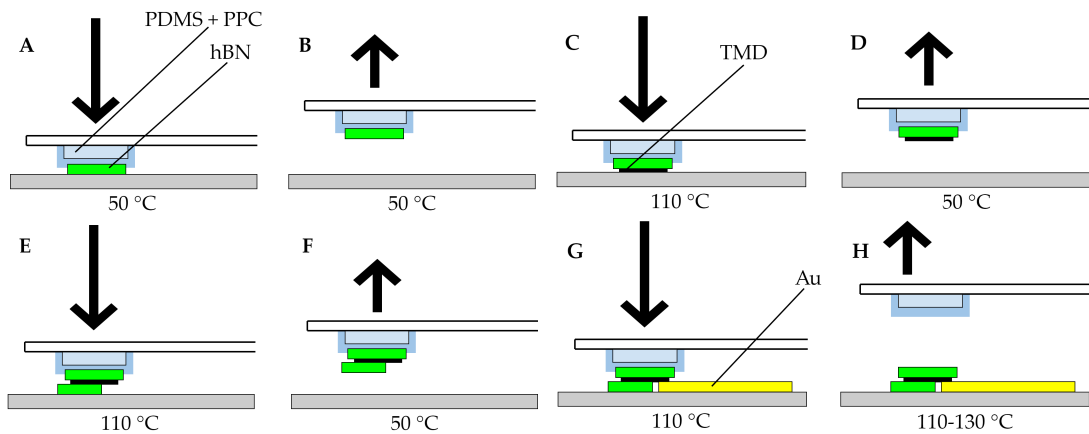


Figure 4.6: Stamping process: "Hot pick-up and stamping" is based on strong van-der-Waals forces between hBN and TMDS as well as the control of adhesion between PPC and hBN using temperature. Flakes of hBN are picked up from a si/sio<sub>2</sub> substrate at 50 °C and can be dropped at a temperature around 110 °C, when the PPC film on the PDMS block loses viscosity. Because thin TMD flakes like mono- and bilayers adhere to hBN much better than to their substrate, the pick-up is highly reliable and arbitrarily high heterostructures can be built. To establish an electrical contact to a layer of the stack, part of it has to lay free, facing down. In this configuration the stack is simply dropped on the edge of the gold structure.

solvents and polymer films to lift the grown flakes off their initial substrate [43]. The advantage of the exfoliation method in this regard is that flakes can be put on any substrate directly from the adhesive tape and do not encounter potentially damaging chemicals. This led to the invention of "viscoelastic stamping", where the TMD-material is exfoliated on a substrate of viscoelastic polymer called polydimethylsiloxane (PDMS)[44]. This so called "stamp" can be brought in contact with the target substrate and peeled off carefully to drop down the flake at a desired position, opening up the possibility of producing carefully designed van-der-Waals heterostructures deterministically.

This method however can exclusively be used to drop TMD flakes, exfoliated directly on the stamp. This is limiting in a number of ways, since exfoliation on a polymer like PDMS comes with unavoidable contamination of the sensitive samples, that only gets worse with every new layer stacked on top. Attempts to develop more flexible methods to pick up TMDS and other 2D materials from clean substrates failed because van-der-Waals forces between the flake and a substrate like sio<sub>2</sub> could not be reliably overcome with a viscoelastic stamp. That is until hBN was introduced as a more suitable substrate. It turns out, that van-der-Waals forces between hBN and TMDS are high enough to remove them from sio<sub>2</sub> deterministically while a range of polymers can be used that strongly adhere to hBN at an appropriate temperature.

This method is called "hot pick-up and stamping"[37, 45]. The stamp used in this process is a block of PDMS, mounted on a glass slide with transparent adhesive tape. The active polymer however is polypropylene carbonate (PPC), that is spin-coated onto the PDMS-block to form a

#### *4 Fabrication of field effect structures*

thin, adhesive coating. PPC, as a polar polymer sticks best to other hydrophilic substances. Therefore if the hydrophobic PDMS is coated with PPC without additional treatment it can peel off, when in contact with  $\text{SiO}_2$ , especially at higher temperatures. However, the adhesion can be greatly enhanced by exposing PDMS to oxygen plasma[46]. Before spin-coating all stamps were treated in a plasma-etching system (Gigaetch 3000) for 20 minutes, at 200 W of power.

The TMD and hBN-flakes are exfoliated on a Si/SiO<sub>2</sub> substrate. To raise adhesion with the flakes, these substrates are treated in oxygen plasma as well (180 s at 200 W). The primary criteria for finding the right hBN-flakes is the flatness of its surface, so that the TMD-flake can be encapsulated between two large terraces without cracks or steps. To allow a fast fabrication process, this flatness is only judged with help of an optical microscope. More sophisticated methods like atomic force microscopy can be used to verify the flatness more accurately. This is however much more beneficial, if the thickness of the hBN plays an important role, for example when it is used in an optical microcavity [20].

The goal of the hot pick-up is now to use a hot-plate to control the van-der-Waals forces between hBN, TMDS and the substrate to ensure adhesion between the parts of the heterostructure as well as to reduce contamination with water molecules from the ambient air.

After all precursors are prepared on Si/SiO<sub>2</sub> substrates, the actual pick-up and stamping process can be carried out. The fabrication setup can be seen in figure 4.5 and a the process in 4.6. The first step is the pick-up of the top hBN flake. At 50°C the van-der-Waals forces between hBN and PPC are already strong enough to lift the flake off the silicon substrate. Bringing flake and PPC in contact at a higher temperature can help as well, because this reduces the polymers viscosity. When cooling down to 40°C to 50°C afterwards, it becomes more rigid again and sticks to the hBN more easily. In the next step the hBN is dropped on the TMD-flake. At a higher temperature of 110°C PPC becomes almost fluid and peels off hBN with ease. While the adhesion between thin TMD flakes and hBN are strong enough to facilitate a pick-up also way below that temperature, heating the substrate during the drop helps to reduce the contamination with droplets of water. Since both TMD and hBN flakes are prepared on clean wafers, humidity in the ambient air of the clean-room seems to be the biggest concern. Raising the temperature above the boiling point both minimizes the formation of actual droplets and also makes blisters of humid air and other contaminants at the hBN-TMD interface more mobile. Dropping the stamp very slowly therefore helps to push these blisters out to the edge of the substrate[37]. The stack of TMD and hBN can then be picked up again following the same procedure that was used for the bare hBN flake. By repeating both steps of pick-up and drop-down an arbitrary number of layers can be added to the heterostructure. In this case it is dropped down on the bottom hBN flake. To contact the TMD flake to gold part of it has to remain outside the hBN encapsulation. This part does not necessarily have to be a monolayer but can also be any form of TMD , that is in contact with it so charges can be transported. The hBN on the other hand is elastic enough so that thicker material does not affect the encapsulation of mono- or bilayer regions.

The last step is to transfer the whole stack to its final position in contact with the electrodes. This is accomplished by repeating the pick-up process once again and dropping the stack in contact with the gold structure.

Despite the strong plasma treatment of the PDMS-stamp in some cases the PPC can peel off during the drop down part of the transfer due to high heat as the polymer becomes ever more liquid. In this case the sample can be carefully treated in a bath of acetone, which dissolves

the polymer rapidly. The sample should stay in the bath for around one minute without any mechanical stress. Afterwards it has to be cleaned in isopropanole and blown dry with nitrogen gas.

#### 4.4.1 ANNEALING

While the hot pick-up should in theory ensure a hBN-TMD interface free of contamination, especially contamination due to humidity in the ambient air can remain between the layers and seriously lower the quality of the sample. To remove this pollution, the sample can be annealed[47]. During annealing, the sample is placed in an annealing oven. While maintaining a high vacuum of  $10^{-3}$  mbar, the oven heats the sample to 250°C for three hours. The vacuum ensures that any volatile materials like water vapor dissipate, while the high temperature increases the mobility of water and eventual polymer contamination on the surface. While not all dirt completely evaporates, the annealing procedure results in the formation of tiny bubbles, so that most of the interface remains clean while all dirt packs at a few avoidable places. Other recipes, that use higher or lower temperatures or longer annealing times can work just as well. Water contamination from the ambient air is still the biggest concern, so even mild temperatures should have a clear advantage over not performing the annealing-step at all. More aggressive recipes, that work at higher temperatures or for longer times can be more effective regarding polymer contaminations that arise from contact to the stamp. If the sample had to be freed of the residual PPC layer with acetone, contamination with polymer molecules is possible. When this exposure can be avoided however, raising the temperature has a limited advantage over milder annealing conditions, but raises also the risk of damaging the sample through temperature induced strain, that can potentially rip the TMD flakes.

### 4.5 ELECTRICAL CHARACTERIZATION

To assess the quality of the the gate structure, its breakdown voltage has to be determined. This is the voltage between top gate and back gate, at which the leakage current starts to rise exponentially by forming conducting channels through the dielectric, that are self-sustaining and lift the conductance permanently[48]. This breakdown voltage is complicated to predict, as it is a nonlinear effect mainly caused by faults in the  $\text{SiO}_2$  layer. Thus it does not only depend on the thickness of the dielectric but also on the area of the top gate, because the statistical chance of encounterin a fault in the material and a conducting channel forming is higher the more area of the sample is covered with conducting material. Additionally the rather violent ohmic contacting of the backgate can also damage the dielectric and lower the breakdown voltage. Therefore each sample has to be classified before being used to tune the charge density in optical spectroscopy. The dielectric in samples used throughout this thesis had a thickness of 50 nm or 90 nm, corresponding to a predicted breakdown voltage of 47.5 V or 85.5 V respectively. To verify these values, the leakage currents have to be monitored while ramping up the voltage. Before breakdown these currents are of the order of 100 pA to 1 nA and can be measured using a lock-in amplifier. A diagram of the circuitry is drawn in figure 4.7. A constant voltage across the desired range of operation ( $\pm 30\text{V}$ ) is added to a small AC-voltage of small amplitude ( $U_0 = 10\text{ mV}_{pp}$ ,  $f = 77.1\text{ Hz}$ ). The amplifier can monitor the real and imaginary part of the current.

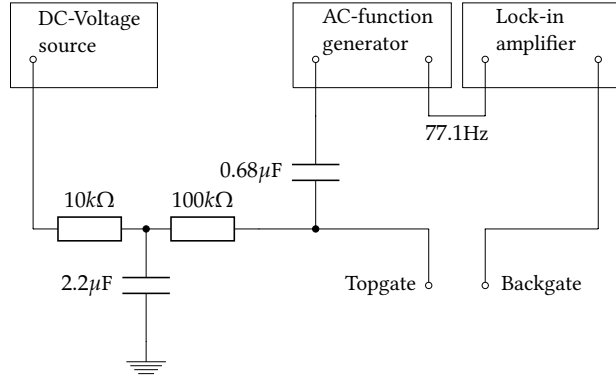


Figure 4.7: Diagram for the cv-measurement. Using a lock-in amplifier and a small AC voltage even very small resistive currents leaking through the samples dielectric can be measured. This way, the maximum DC voltage at the gate can be obtained, by ramping a DC voltage source until the resistive current starts to rise exponentially.

The real part is the resistive current, or leakage, that flows through the samples dielectric. The imaginary part is proportional to the capacity. By first performing the experiment with a gauge capacitance, the capacity of the sample can be measured with high precision. For the purpose of characterizing the dielectric however, the resistive current is the more interesting quantity. To find the breakdown voltage the DC-voltage is ramped until the leakage rises exponentially. At this voltage, the resistive current is still usually still below a few nA—small enough to not inflict permanent damage to the dielectric and marks a safe range of positive and negative voltages the device can be operated on during the experiment.

## 5 SPECTROSCOPY OF WSe<sub>2</sub> GATE DEVICES

The goal of this thesis was to advance tools that can help understanding the optical spectra of TMD monolayers. In this chapter the experimental tools and results will be discussed in more detail. The narrow linewidth of the spectral features due to hBN encapsulation enables the possibility of analyzing the lines of the optical spectrum individually. This is accomplished by tracking their position and shape though different charge densities and magnetic field strengths. The measurements, discussed in the coming chapter are all performed on a sample of tungsten-diselenide (wSe<sub>2</sub>). Tungsten-based TMDS are of particular interest, because their complex band-structure yields a rich spectrum, that is still poorly understood.

### 5.1 OPTICAL SETUP

The optical setup is a confocal microscope. This means that the sample is placed in the focal plane of a low temperature objective and instead of capturing a wide field image of the sample only the signal from the focal point is collected. With a high quality objective the spot is only limited by the fundamental diffraction limit, yielding high spatial resolution. The other advantage is the high ratio between excitation power and collected signal, which puts lower limits on integration times and the signal to noise ratio. A diagram of the complete setup can be seen in figure 5.1. The excitation beam from a laser is guided to the so called excitation arm with a single mode optical fibre. It passes through a linear polarizer to define a polarization axis and is reflected to the objective by a beam-sampler. To analyze circular dichroism in the detected beam, it passes through a quarter waveplate and another linear polarizer before being coupled into another optical fibre, that is connected to a spectrometer. The sample is mounted on a piezo nanopositioner inside a cryostat or container of liquid helium and connected to a voltage source, to tune the charge density in the TMD flake. A strong, homogenous magnetic field along the z-axis of the sample can be supplied by a superconducting magnet.

For PL spectroscopy, the sample is excited by a laser beam with a narrow frequency profile and high power. Because this beam has a much higher intensity, than the collected PL it is tuned to a higher frequency than the main exciton resonance, to obtain a complete spectrum without features from the excitation beam. To avoid stray light inside the spectrometer a longpass filter additionally blocks the laser before entering the detection fiber. A shortpass filter in the excitation arm blocks Raman modes of the optical fiber, a result from high excitation power, that can have frequencies overlapping with the PL of the sample. When the setup is operated for reflection spectroscopy these filters are omitted. Instead, the sample is illuminated with a broad band white light source at a low power. To find the signal, a background spectrum, recorded in absence of the TMD flake is subtracted from the main spectrum.



Figure 5.1: Optical setup for confocal spectroscopy: Light from a **laser**-source is guided to the setup in a single mode optical fibre and collimated. To cut off raman-modes, that are created in the fibre a **shortpass** filter is installed behind the collimator. A **linear polarizer** defines a polarization axis. A **beam-sampler** is reflecting the excitation beam into a **low temperature apochromat**, whose focus lies on the sample, with a spotsize of  $\sim 0.5\mu\text{m}$ . The sample is mounted on a **piezo nanopositioner**, that is placed inside a **cryostat** at a temperature of up to  $3.1\text{ K}$  or in a container of liquid helium at  $4.2\text{ K}$ . The cryostat is equipped with a **superconducting magnet** that can supply a homogenous magnetic field up to  $9\text{ T}$ . The sample electrodes are connected to a **voltage source** (Yokogawa) that supplies  $\pm 32\text{V}$ . The detection spot is identical with the excitation. The reflection or photoluminescence is collimated again in the objective and passes through a  $\sigma^-/\sigma^+$ -analyzer consisting of a **quarter waveplate** and a **linear polarizer**, before being focussed in the detection fibre that connects to a **spectrometer**. A **camera** can be used to monitor the spot and image the sample, if it is brought out of focus.

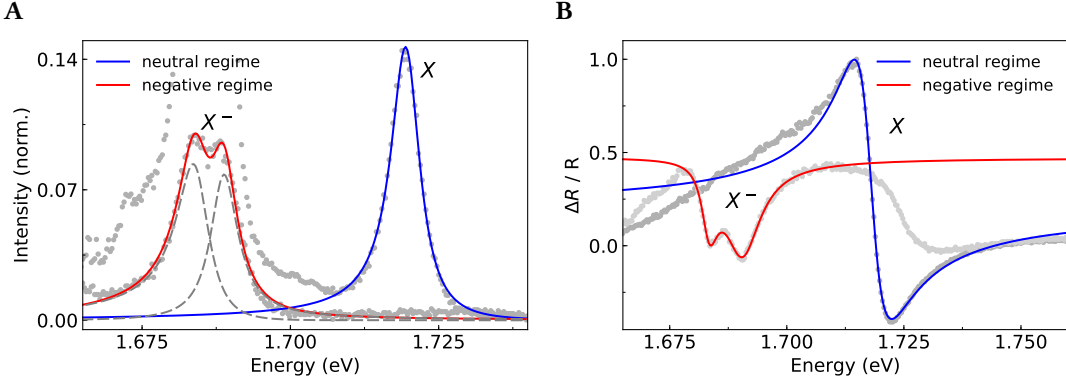


Figure 5.2: Fits of the exciton ( $X$ ) and trion ( $X^-$ ) features in a neutral and negatively charged spectrum. **A PL**: The lineshape in the fitting model is a lorentzian with adaptive linewidth to model the slight asymmetry of the peaks. It is tuned with a sigmoid function, according to a symmetry parameter. The double-peak of the trion feature is a sum of two asymmetric lorentzians. **B Reflection**: The exciton resonance in this hBN encapsulated sample does not show a clean dip and can be approximated by a model function corresponding to the scattering cross section of a fano resonance. The trion double dip can be fitted using a sum of two asymmetric lorentzians. However, in contrast to the PL fit, a constant shifting parameter is added, and the starting values for the scaling parameter are chosen negative.

$$S_R = \frac{\Delta R}{R} = \frac{R_{\text{flake}} - R_{\text{background}}}{R_{\text{background}}} \quad (5.1)$$

The signal  $S_R$  is the difference of the Reflection signals of TMD flake and background. The division by the background reflection is made to normalize the signal. The resulting reflection spectrum should show only features, of the flake. In practice, the obtained data has to be evaluated with some precautions in mind, to avoid misidentifying for example interference effects due to differences in hBN thickness as features of the absorption behavior of the sample.

## 5.2 MODELLING PEAK SHAPES

To precisely quantify positions and linewidths of the spectral features, they have to be modelled using appropriate fitting functions. In PL all peaks should ideally have a lorentzian line shape (see Figure 5.3 A).

$$i(\nu) = \frac{a}{1 + \epsilon^2} \quad (5.2)$$

$$\epsilon = \frac{\nu_0 - \nu}{\gamma/2} \quad (5.3)$$

where  $I$  is the intensity,  $\epsilon$  is the reduced energy, composed of the energy  $\nu$ , the peak position  $\nu_0$  the linewidth  $\gamma$  at FWHM. For a maximum value  $a$  of 1, the function is normalized. In the

crowded spectrum of an imperfect sample however, this is only an approximation, as the different peaks blend together and can have fine structures, that cannot be resolved as individual features. This leads not only to a broadening of the lines, but also skews the line shape, mostly resulting in a “red shoulder” – higher intensity towards the low-energy end of the peak. To accurately model these features and get good estimates for peak positions as well as linewidths the lorentzian has to be expanded. A generic way of modelling an asymmetric line, that is close to the “natural” linewidth is using a lorentzian with variable linewidth  $\gamma$ , meaning the static linewidth of in 5.3 is replaced by a smooth sigmoid function, that includes an additional symmetry parameter[49].

$$\gamma = \frac{2\gamma_0}{1 + e^{k(\nu - \nu_0)}} \quad (5.4)$$

This value is then inserted into (5.3). The symmetry parameter  $k$  scales the steepness of the curve sigmoid function and thus the skewedness of the lineshape. The  $\gamma_0$  parameter is identical to  $\gamma$  at  $\nu_0$  and corresponds to the peaks linewidth. For  $k = 0$  (5.3) collapses to  $\gamma_0$  and the standard lorentz lineshape is recovered. The asymmetric lorentzian can be used to model all peaks in the PL spectrum.

In reflection spectroscopy, the signal should correspond to the absorption of the sample. Therefore the straight forward way to model features would base on a lorentzian function as well, only with a negative sign<sup>1</sup>. However, in an hBN-encapsulated sample, the spectrum can be more complicated (see Figure 5.4). The neutral exciton resonance has a highly asymmetric lineshape, that cannot be modeled by a bare lorentzian (either (5.3) or (5.4)). A more general function is the lineshape of a fano resonance. The physical background is the interference between a resonance and a continuous background[50]. In case of encapsulated TMD monolayers, this lineshape stems from the hBN layer, that forms a microcavity with the underlying reflective si/sio<sub>2</sub> substrate[51].

$$\frac{(q + \epsilon)^2}{(1 + \epsilon^2)} = 1 + \frac{q^2 + 2q\epsilon - 1}{1 + \epsilon^2} \quad (5.5)$$

where  $q$  is the so-called fano parameter. This can be seen as a more general form of (5.3). For  $q = 0$  the shape of (5.5) reduces to a downwards facing lorentzian. Just like for the trion and all PL features, the linewidth parameter for (5.4) can be deployed to skew the function to better fit real data.

The trion signal in the charged spectrum shows a double dip. While the physical process would demand a fano-type model just as for the neutral exciton, the close proximity of both signals and the strong background complicate the correct estimation of the peak position. Therefore a negative asymmetric lorentzian is the naive but effective choice. To compensate for the strong background of the neutral resonance, a constant parameter is added, that gives the peaks a positive offset. Examples of the fitting process for reflection and PL spectra can be seen in figure 5.2. To use the explained fitting functions, the data was sliced to isolate and fit each feature. This makes the minimum and maximum in the energy scale additional parameters that in practice strongly influence the convergence behaviour of the fitting algorithm.

---

<sup>1</sup>The sign of the fitting functions depends on the definition of the spectrum itself. In this work, the background is subtracted from the signal, yielding the reflection off the flake. A flipped sign on the other hand corresponds to the absorption.

### 5.3 Wse<sub>2</sub> spectrum at different doping levels

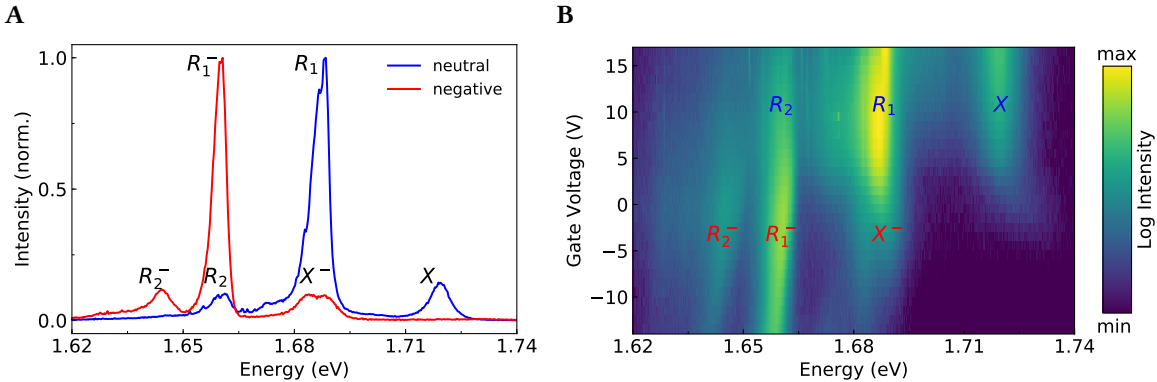


Figure 5.3: Photoluminescence of wse<sub>2</sub> at different doping levels. **A** Spectra in the neutral and negatively charged regime. The PL of the exciton (X) is clearly visible at the blue end of the spectrum. The replica peaks ( $R_1$ ,  $R_2$ ) correspond to acoustic phonon sidebands of  $Q$ - and  $K'$ -indirect excitons with low-intensity features to the red indicating optical sidebands. In a negatively charged regime, they vanish in favor of redshifted peaks, that correspond to the trion ( $X^-$ ) that is split by electron-electron exchange interaction, and its momentum indirect counterparts. While  $R_1^-$  fits the picture as an acoustic sideband of  $X^-$ ,  $R_2^-$  seems to be the charged spin-unlike dark state. **B** Spectral features in a gate-sweep. The plot can be devided into a neutral and charged regime below and above 5V. This threshold is a signature of unintentional n-doping and varies across the sample.

However, the disentanglement of the individual peaks makes it easier to finetune the models parameters, such that the most accurate estimate can be found.

## 5.3 WSe<sub>2</sub> SPECTRUM AT DIFFERENT DOPING LEVELS

In all semiconductors the density of free charges through intentional or unintentional doping strongly influences its behaviour. TMD samples very often exhibit unintentional doping[52, 53]. Additionally other defects of different nature leave marks in the optical spectrum [54, 55]. The discussion and interpretation of the spectrum thus becomes harder and highly speculative in samples prepared without control of the charge density. Gate-tunability therefore becomes a necessary tool to establish a ground truth for a neutral sample but also to study the spectrum in charged environment intentionally.

### 5.3.1 PHOTOLUMINESCENCE SPECTRUM

The PL spectrum is pictured in figure 5.3 both in a neutral and charged regime. The sudden change in the spectrum at 5 V shows, that at this point on the sample, the TMD-flake is negatively doped. As a result only the neutral and negative regime could be studied. The peak to the blue end of the spectrum belongs direct spin-like neutral exciton (X). This peak is well un-

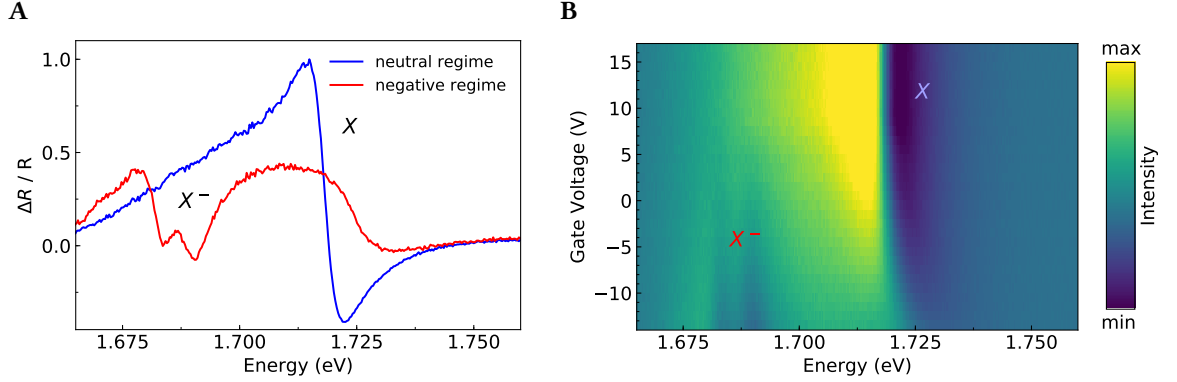


Figure 5.4: Reflection of wSe<sub>2</sub> at different doping levels. **A** The reflection spectrum of wSe<sub>2</sub> in a neutral and negatively charged regime. The neutral spectrum shows a strong response, corresponding to the main exciton resonance (X). The absorption of the exciton almost vanishes in the charged spectrum and a double dip appears, that corresponds to the trion resonance, resolving the typical exchange splitting (X<sup>-</sup>). **B** Reflection spectra at different voltages. The exciton absorption shows a similar response as in PL, however stretched to lower voltages. The absorption at the trion resonance can be resolved much better, than the corresponding peaks in PL .

derstood and can therefore be used to benchmark the spectral linewidth and the overall quality of the sample. With a linewidth of 6.8 meV the exciton is still above the intrinsic homogeneous linewidth which is reported to be below 2 meV[56, 57]. Inhomogeneous broadening can be mostly attributed to local changes in the potential landscape that can arise from defects, impurities as well as strain induced shifts in the band structure[58]. The diffraction limited spot of the objective is large enough to cover a large ensemble of slightly different contributions to the PL signal, that merge to a broad peak. Apart from the FWHM linewidth of the exciton peak, both a significant asymmetry parameter in the fit as well as a slight deviation from the lorentzian line-shape are indicators, that the feature has an considerable substructure and there is still room for improvement in terms of sample fabrication.

However, the linewidth-limited resolution of the present sample is good enough to distinguish the fine splitting of the trion peak in the charged regime (X<sup>-</sup>). When the gate voltage is tuned, the Fermi level is shifted. The negative regime is reached when the Fermi level rises above the lower K and K' valleys in the conduction band and free charge carriers enter the flake. Optically excited excitons can bind electrons from either of the two valleys resulting in two a-priori degenerate trion states, that differ energetically because of a difference in Coulomb exchange interaction [19]. The resulting splitting can be resolved in the present sample and has a value of 5.2 meV. The spectral difference to the exciton peak in the neutral regime gives an estimate of an additional trion binding energy. Taking into account the exchange splitting it has a value of 30.5 - 35.8 meV. Since the separation of the two trion peaks is quite low, the linewidth estimates from the fit are only a rough estimate but are close to the neutral exciton at 5-7 meV.

The peaks to the red in both the neutral and charged spectra can be explained using the phonon sideband model described in 2.3.1. The  $Q$ -indirect exciton should lie above the direct spin-unlike state. Therefore it makes sense to identify the intense  $R_1$  peak with its acoustic sidebands, putting the  $Q$ -exciton roughly  $19 \pm 2$  meV below  $X$ . The optical sidebands coincide with a low intensity bump that fits the predicted energies. The direct spin-unlike exciton ( $D$ ) should be 40 meV to the red of  $X$ , but cannot be resolved clearly, possibly because  $R_1$  is broad and intense enough to merge with the weak PL of  $D$ . Its momentum-indirect counterpart in  $K'$  should have the same energy, thus we can estimate its phonon sidebands, which fit the strong  $R_2$  peak and the corresponding low-intensity feature to the red.

Assuming the nature of the phonon sidebands does not change fundamentally in a charged environment it is worth a try to treat the charged spectrum in a similar fashion. Analogous to the trion, the energy of the peaks should redshift upon interaction with free charge carriers. When shifting the  $Q$ -valley by the trion binding energy, it fits the two most intense replica peaks in the charged spectrum ( $R_1^-$ ,  $R_2^-$ ). However,  $R_2^-$  also matches  $D$  shifted by the trion binding energy. This could explain the relatively strong signal at this energy. The weak feature to the red could then charged acoustic replica of  $K'$ .

### 5.3.2 REFLECTION SPECTRUM

The reflection spectrum offers a way to quantify a materials absorption. In TMDS it can therefore offer a way to disentangle exciton resonances from states, that form by their non-radiative decay. These include the discussed phonon sidebands but also defect states and quantum dots, that have low absorption but brighten up trapped excitons[59]. The reflection spectrum therefore offers a more “pure” view on the direct exciton and the charged trion. The reflection spectrum can be seen in figure 5.4. The neutral spectrum shows a clear signature of the direct exciton resonance ( $X$ ). This spectral feature in an hBN encapsulated sample has the shape of a fano resonance, because of interference effects. The TMD-hBN heterostructure acts as a microcavity and shows very high reflectivity at the resonance frequency[51]. Upon tuning the gate to negative voltages, the absorption and reflection at the exciton resonance is suppressed and the trion resonance forms ( $X^-$ ). Just like in PL this resonance exhibits a splitting due to coulomb exchange energy.

## 5.4 MEASURING THE VALLEY ZEEMAN EFFECT

As described in section 2.4 the band gap and exciton energies in TMDS shift when exposed to an out-of-plane magnetic field. These shifts are reversed in light of opposite helicity and differ for different types of excitonic processes. Measuring the splitting, and quantifying it through the  $g$ -factor can yield a deeper insight in the nature of the spectral features. Figure 5.7 and 5.8 show the PL and reflection spectra for different gate voltages at 0 and 8 T. Because of different magnetic shifts of the different peaks, looking at  $\sigma^+$  and  $\sigma^-$  polarized spectra at high magnetic field can help to resolve features, that are otherwise hidden by inhomogeneous broadening. The first interesting feature to study in this fashion is the two trion peaks ( $X^-$ ). At 8 T they reveal significant change in their splitting, merging to one peak in  $\sigma^+$  while showing a clear

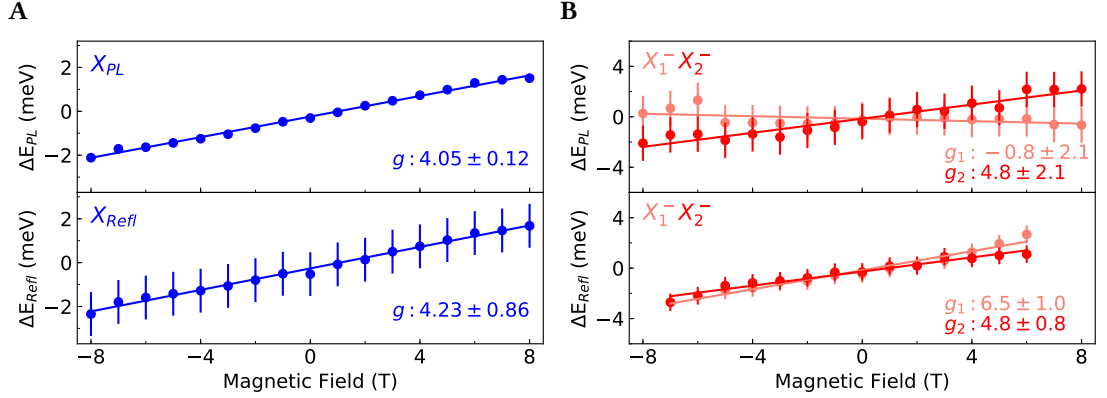


Figure 5.5: Exciton valley splitting in PL and reflection. **A** The  $g$ -factor of the neutral exciton is in good agreement with previous studies. The fit of the reflection measurement has a large error bar, because of the complicated lineshape. Since the variance of the data points is low, this seems to be a systematic error. **B** The trion peak can only be reliably modeled in the reflection spectrum because of insufficient signal-to-noise ratio and limitations of the linewidth. The fits suggest a different  $g$ -factor for the two subfeatures.

splitting in  $\sigma^-$ . As will be discussed later on, this difference is so far unaccounted for but may be coupled to the asymmetry in intensity when the gate-voltage is swept.

The trion fine structure is a result of electron-electron exchange interaction. The singlet-state consists of an exciton and an electron of opposite spin at the  $K$ -point while the triplet state involves an additional electron in the  $K'$ -valley, but with the same spin component as the electron in the exciton. The spin-parallel triplet state has a lower binding energy, which allows to also observe the different behavior with regards to the charge density. At high negative gate voltages, both peaks are less intense with the blue peak losing signal much more rapidly. The reasons for that are speculative at best. Recent measurements in ws<sub>2</sub> point to the singlet state being stable only at low temperatures[60]. Similarly, the triplet state in wse<sub>2</sub> could be more sensitive to large densities of free charge carriers. How this connects to their difference in magnetic moment is unclear.

#### 5.4.1 G-FACTORS

The magnetic splitting  $\Delta E$  can be quantified by the  $g$ -factor. Because  $\Delta E$  is linear in magnetic field strength  $B$ , the peak positions can be fitted using simple linear regression where the slope is connected to the  $g$ -factor in the following fashion:

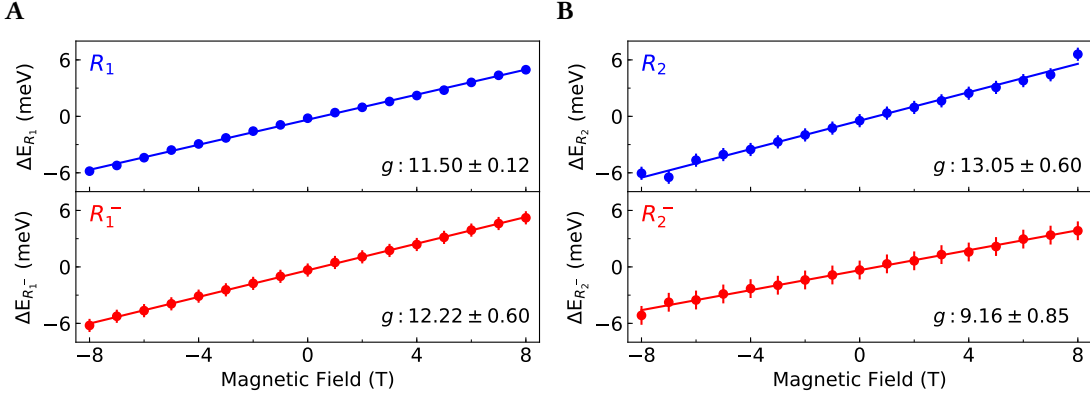


Figure 5.6: Valley splitting of phonon replica. **A** The intense  $R_1$  peak and its charged counterpart  $R_1^-$  show a similar  $g$ -factor, suggesting the same origin. This is consistent with the proposed model, that identifies the peaks as acoustic sidebands of momentum-indirect excitons in the  $Q$ -valley.  $R_1$  is of particular interest, because this feature conventionally is attributed to the trion. The strong difference in the  $g$ -factor however suggests a different origin than the trion feature, even though they share the same energy in the spectrum. **B** The neutral peak  $R_2$  was previously identified as a phonon sideband of the  $K'$ -indirect exciton. The high  $g$ -factor however does not offer a direct argument to support this assumption. However, the charged counterpart  $R_2^-$  has a similar  $g$ -factor as was previously measured for  $D$ , which underscores the assumption of the feature being the charged spin-unlike exciton in  $K$ .

$$g = \frac{1}{\mu_B} \underbrace{\frac{\Delta E}{\Delta B}}_{\text{slope}} \quad (5.6)$$

$$\Delta E = E_{\sigma^+} - E_{\sigma^-} \quad (5.7)$$

Because the splitting is a lot smaller than the linewidth—0.25 meV / T at a linewidth of 7 meV—the peaks have to be fitted using the procedures described in 5.2 to obtain a low error and therefore an accurate estimate for the  $g$ -factor. Not all features can be resolved well enough, because of either a bad signal to noise ratio or linewidth-related blending with other peaks.

The  $g$ -factor of the neutral exciton and trion resonances can be measured in both PL and reflection spectroscopy (see figure 5.5). This helps to cross-check experimental results. In case of the neutral exciton, both methods yield a  $g$ -factor that aligns well with many previous studies [29, 61–63] and also with each other. The fits of the reflection spectra carry a relatively high error. The error bars were estimated by eye using plots to determine deviation of the lineshape from the peaks maxima and minima. Because these errors are much higher than the standard deviation it is fair to say, that they only provide a coarse upper bound. They most likely origin from the substantial deviation of the lineshape from the ideal fano-resonance on the blue and red shoulder.

The trion resonance is much more easy to measure in reflection. The reason for this is partly the bad signal to noise ratio of its PL signal, that can be linked to the longer lifetime of the charged state[64]. But another factor seems to be the limited resolution due to the linewidth of the peaks. The two peaks in the reflection spectrum are separated by roughly 2 meV more, than in PL. The reason for that could simply be the fact, that the lorentzian fit does not really reflect the proper lineshape in the reflection spectrum. Fitting the trion absorption with a double fano lineshape could possibly resolve this difference. For the calculation of the g-factor this should however not make a difference.

While the trion fits carry a significant error—also in reflection—they clearly show a different g-factor for each of its features. Since the decay of the trion leaves one free electron behind, it makes sense, that the trion features show the same g-factor as X. Nonetheless, this difference has also been observed in ws<sub>2</sub> samples at even higher magnetic fields, suggesting a non negligible influence of the excess electron towards the total magnetic moment[61].

Having the uncertainty in mind we can compare the trion g-factor to the strong  $R_1$  peak in the neutral spectrum (see figure 5.6). Because it has the same energy as the trion, it is easy to misidentify both features as the same peak and attribute them to the trion. Especially if the sample has no gate control intrinsic electron doping offers a qualitative but not accurate argument for this identification. The magnetic field measurements however show a clear difference between their respective valley splitting. As stated the g-factor of the trion is hard to determine in PL and has a large error. However, it is bound between 0 and around 6 which is half of the g-factor of  $R_1$ . The strong mismatch can also be observed qualitatively in 5.7.

Unfortunately this leaves the question about the origin of the high g-factor of  $R_1$ . As briefly discussed in section 2.4 the momentum indirect exciton in Q should not have a g-factor at all, when only looking at the orbital and spin contributions. The effective mass for electrons at the Q-point has however not been calculated for this thesis and therefore the theoretical model predicting the g-factor still has to be completed. This is similar for the  $K'$  indirect exciton and the corresponding peak  $R_2$ , that should be composed of its acoustic phonon sidebands. When counting the orbital and spin contributions it should have the same g-factor as X. That this is not the case means, that a more thorough theoretical understanding is necessary to verify or falsify the identification of the peak.

When looking at the charged spectrum the g-factor of  $R_1^-$  matches that of  $R_1$  within the  $2\sigma$ -range. Because their distance in energy to X and  $X^-$  also fits it is reasonable to regard the peaks as neutral and charged version of the same momentum-indirect exciton in Q.

As discussed in the previous section the second peak  $R_2^-$  energetically matches the spin-unlike but direct dark exciton D. Therefore it is no wonder, that this is reflected in the significantly smaller g-factor with respect to the phonon sideband peaks. While it is higher than the value predicted in section 2.4 it is close to what was reported for the neutral dark exciton[17].

## 5.5 COMPARISON TO BILAYER WSE<sub>2</sub>

As pointed out in section 2.5, bilayer wse<sub>2</sub> has an indirect band gap and most of the weaker PL can be attributed to the decay of momentum-indirect excitons.

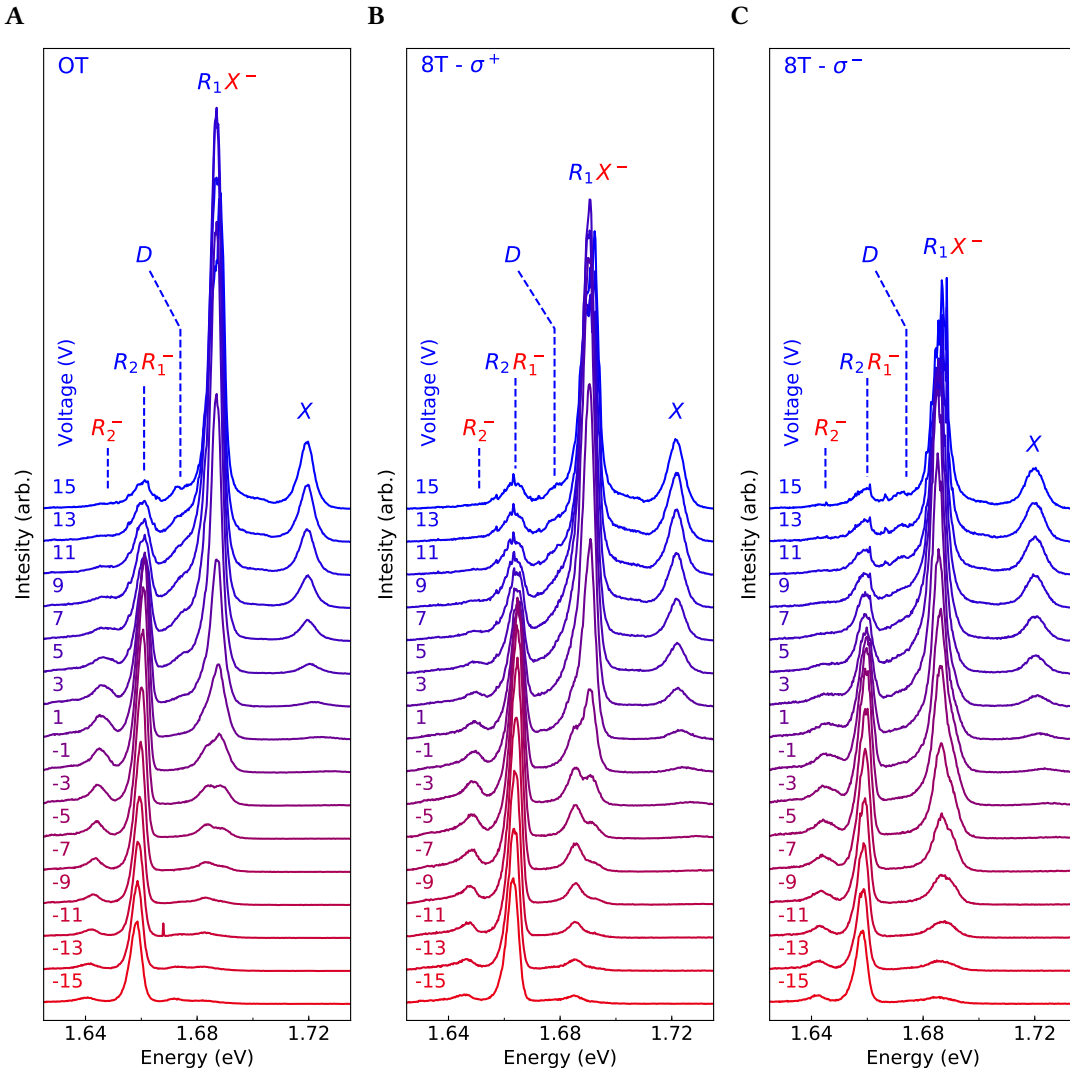


Figure 5.7: PL spectra of wse<sub>2</sub> at high magnetic fields for different gate voltages. In the neutral spectrum the dark exciton ( $D$ ) lies too close to the strong phonon sideband  $R_1$  to be resolved clearly. The strong splitting of this feature reveals  $D$  more clearly in the  $\sigma^+$ -polarized spectrum at 8T (gfactor). The trion peak in the negative regime is composed of at least two features. As can be seen these peaks have different g-factors as well, that lead to a wide split in  $\sigma^+$  and merge to one feature in  $\sigma^-$ .

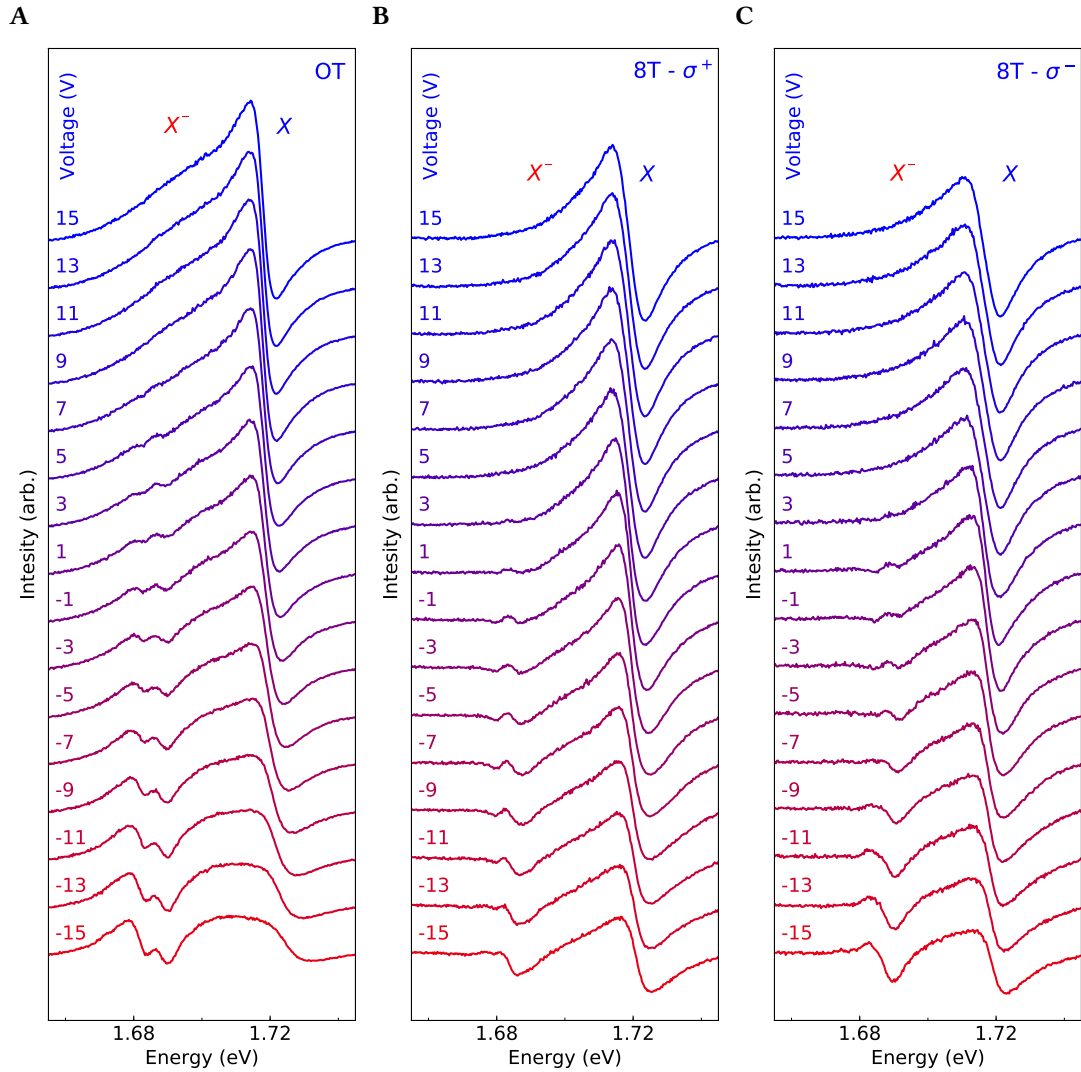


Figure 5.8: PL spectra of wse<sub>2</sub> at high magnetic fields for different gate voltages. In the neutral spectrum, towards the positive end, the replica peaks  $R_1$  and  $R_2$  get significantly skewed at 8 T, pointing towards several underlying peaks with different  $g$ -factors. The trion peak in the negative regime is composed of at least two features. As can be seen these peaks have different  $g$ -factors as well, that lead to a wide split in  $\sigma^+$  and merge to one feature in  $\sigma^-$ .

## 6 SUMMARY & OUTLOOK

The goal of this thesis was to establish a fabrication pipeline for narrow linewidth TMD monolayers, encapsulated in hBN, embedded in a gate-structure. This was accomplished by combining the dry transfer technique of “hot pick-up and stamping” with contact lithography and mechanical exfoliation.

TMD monolayers were produced by mechanically exfoliating material from a bulk crystal with adhesive tape. To obtain narrow linewidths they were encapsulated in hBN flakes by picking up hBN and TMD flakes one by one with a PPC-coated PDMS-stamp and dropped in contact with lithographically written gold wires. To verify the function and determine the maximum gate voltage the leaking current through the samples was measured using a lock-in amplifier.

A combined gate-tunable mono- and bilayer sample of tungsten diselenide was analyzed by means of confocal laser spectroscopy. Both reflection and photoluminescence spectra were taken while sweeping the gate voltage to determine intrinsic doping and observe the transition between neutral and negative charge carrier density.

The observed spectral linewidth of 6–7 meV for the neutral exciton peak are a significant improvement over previous samples, especially because these values can be observed on most of the sample. However, because the intrinsic homogenous linewidth is believed to be only a third of this value, there is still room for improvement.

Nevertheless, the good linewidth-related result helped to gain insight about the origin of the different spectral features as gate voltage sweeps were repeated for high positive and negative magnetic fields. The observed g-factors were used to distinguish between the negatively charged trion state and a not yet fully understood strong feature in the neutral spectrum and their related lower energy peaks.

The g-factors of previously unidentified peaks could help to verify our model, that identifies them as phonon replica of momentum-indirect excitons. However, this will have to be completed by other measurements including life-time measurements, power dependence but most of all theoretical predictions of g-factors. The same procedures can also be performed on other TMDS—for example the closely related  $ws_2$ . During the work for this thesis, a sample of  $ws_2$  with an optimal gate-tunability was already produced and can be analyzed in the future.

But there are also possible advancements in the fabrication process and sample engineering. Uncontrolled thickness of the bottom hBN flake as well as the 50–90 nm  $SiO_2$  dielectric mean, that in order to create significant electric field strengths, high voltages close to the breakdown have to be applied to observe the transition between all relevant regimes. Because of negative intrinsic doping only the neutral and negative regime could be resolved in this thesis. However, there are viable options to navigate this limitation. One option is to integrate top and backgate into the heterostructure itself. Using graphene beneath the bottom hBN flake or above the top the distance between the gates could be substantially lowered. The result would be a much higher field strength close to the monolayer. The other option would be to still use

## *6 Summary & outlook*

the substrate as backgate but to discard  $\text{SiO}_2$  as a dielectric. Using techniques such as atomic layer deposition of materials like aluminum oxide, a similar effect could be achieved, without raising the complexity of the van-der-Waals heterostructure.

But also the present techniques could be used to build new interesting samples. Stacking different TMD monolayers on top of each other to form gate-tunable heterobilayers could yield a better understanding of features like second-harmonic generation and layer-indirect excitons. A challenge would be to align the crystal axis of the precursor monolayers, but this could also be an opportunity to study moiré effects in more detail.

## BIBLIOGRAPHY

- <sup>1</sup>K. F. Mak, K. L. McGill, J. Park, and P. L. McEuen, “The valley hall effect in MoS<sub>2</sub> transistors”, *Science* **344**, 1489–1492 (2014).
- <sup>2</sup>F. Langer, C. P. Schmid, S. Schlauderer, M. Gmitra, J. Fabian, P. Nagler, C. Schüller, T. Korn, P. G. Hawkins, J. T. Steiner, U. Hettner, S. W. Koch, M. Kira, and R. Huber, “Lightwave valleytronics in a monolayer of tungsten diselenide”, *Nature* **557**, 76–80 (2018).
- <sup>3</sup>Q. H. Wang, K. Kalantar-Zadeh, A. Kis, J. N. Coleman, and M. S. Strano, “Electronics and optoelectronics of two-dimensional transition metal dichalcogenides”, *Nature Nanotechnology* **7**, 699–712 (2012).
- <sup>4</sup>D. Xiao, G.-B. Liu, W. Feng, X. Xu, and W. Yao, “Coupled spin and valley physics in monolayers of MoS<sub>2</sub> and other group-VI dichalcogenides”, *Physical Review Letters* **108** (2012) 10.1103/PhysRevLett.108.196802.
- <sup>5</sup>B. Ouyang, G. Lan, Y. Guo, Z. Mi, and J. Song, “Phase engineering of monolayer transition-metal dichalcogenide through coupled electron doping and lattice deformation”, *Applied Physics Letters* **107**, 191903 (2015).
- <sup>6</sup>A. Chernikov, T. C. Berkelbach, H. M. Hill, A. Rigosi, Y. Li, O. B. Aslan, D. R. Reichman, M. S. Hybertsen, and T. F. Heinz, “Exciton binding energy and nonhydrogenic rydberg series in monolayer WS<sub>2</sub>”, *Physical Review Letters* **113** (2014) 10.1103/PhysRevLett.113.076802.
- <sup>7</sup>A. V. Stier, N. P. Wilson, G. Clark, X. Xu, and S. A. Crooker, “Probing the influence of dielectric environment on excitons in monolayer WSe<sub>2</sub>: insight from high magnetic fields”, *Nano Letters* **16**, 7054–7060 (2016).
- <sup>8</sup>S. Borghardt, J.-S. Tu, F. Winkler, J. Schubert, W. Zander, K. Leosson, and B. E. Kardynał, “Engineering of optical and electronic band gaps in transition metal dichalcogenide monolayers through external dielectric screening”, *Physical Review Materials* **1** (2017) 10.1103/PhysRevMaterials.1.054001.
- <sup>9</sup>T. Jakubczyk, K. Nogajewski, M. R. Molas, M. Bartos, W. Langbein, M. Potemski, and J. Kasprzak, “Impact of environment on dynamics of exciton complexes in a WS<sub>2</sub> monolayer”, *2D Materials* **5**, 031007 (2018).
- <sup>10</sup>B. Peng, Q. Li, X. Liang, P. Song, J. Li, K. He, D. Fu, Y. Li, C. Shen, H. Wang, C. Wang, T. Liu, L. Zhang, H. Lu, X. Wang, J. Zhao, J. Xie, M. Wu, L. Bi, L. Deng, and K. P. Loh, “Valley polarization of trions and magnetoresistance in heterostructures of MoS<sub>2</sub> and yttrium iron garnet”, *ACS Nano* **11**, 12257–12265 (2017).

## BIBLIOGRAPHY

- <sup>11</sup>C. Zhao, T. Norden, P. Zhang, P. Zhao, Y. Cheng, F. Sun, J. P. Parry, P. Taheri, J. Wang, Y. Yang, T. Scrace, K. Kang, S. Yang, G.-x. Miao, R. Sabirianov, G. Kioseoglou, W. Huang, A. Petrou, and H. Zeng, “Enhanced valley splitting in monolayer WSe<sub>2</sub> due to magnetic exchange field”, *Nature Nanotechnology* **12**, 757–762 (2017).
- <sup>12</sup>T. Smoleński, M. Goryca, M. Koperski, C. Faugeras, T. Kazimierczuk, A. Bogucki, K. Noga-jewski, P. Kossacki, and M. Potemski, “Tuning valley polarization in a WSe<sub>2</sub> monolayer with a tiny magnetic field”, *Physical Review X* **6** (2016) 10.1103/PhysRevX.6.021024.
- <sup>13</sup>A. Neumann, J. Lindlau, L. Colombier, M. Nutz, S. Najmaei, J. Lou, A. D. Mohite, H. Yamaguchi, and A. Högele, “Opto-valleytronic imaging of atomically thin semiconductors”, *Nature Nanotechnology* **12**, 329–334 (2017).
- <sup>14</sup>N. Zibouche, A. Kuc, J. Musfeldt, and T. Heine, “Transition-metal dichalcogenides for spintronic applications: spintronics beyond graphene”, *Annalen der Physik* **526**, 395–401 (2014).
- <sup>15</sup>Z. Jin, X. Li, J. T. Mullen, and K. W. Kim, “Intrinsic transport properties of electrons and holes in monolayer transition-metal dichalcogenides”, *Physical Review B* **90** (2014) 10.1103/PhysRevB.90.045422.
- <sup>16</sup>J. P. Echeverry, B. Urbaszek, T. Amand, X. Marie, and I. C. Gerber, “Splitting between bright and dark excitons in transition metal dichalcogenide monolayers”, *Physical Review B* **93** (2016) 10.1103/PhysRevB.93.121107.
- <sup>17</sup>C. Robert, T. Amand, F. Cadiz, D. Lagarde, E. Courtade, M. Manca, T. Taniguchi, K. Watanabe, B. Urbaszek, and X. Marie, “Fine structure and lifetime of dark excitons in transition metal dichalcogenide monolayers”, *Physical Review B* **96** (2017) 10.1103/PhysRevB.96.155423.
- <sup>18</sup>G. Wang, C. Robert, M. M. Glazov, F. Cadiz, E. Courtade, T. Amand, D. Lagarde, T. Taniguchi, K. Watanabe, B. Urbaszek, and X. Marie, “In-plane propagation of light in transition metal dichalcogenide monolayers: optical selection rules”, *Physical Review Letters* **119** (2017) 10.1103/PhysRevLett.119.047401.
- <sup>19</sup>E. Courtade, M. Semina, M. Manca, M. M. Glazov, C. Robert, F. Cadiz, G. Wang, T. Taniguchi, K. Watanabe, M. Pierre, W. Escoffier, E. L. Ivchenko, P. Renucci, X. Marie, T. Amand, and B. Urbaszek, “Charged excitons in monolayer WSe<sub>2</sub>: experiment and theory”, *Physical Review B* **96** (2017) 10.1103/PhysRevB.96.085302.
- <sup>20</sup>M. Sidler, P. Back, O. Cotlet, A. Srivastava, T. Fink, M. Kroner, E. Demler, and A. Imamoglu, “Fermi polaron-polaritons in charge-tunable atomically thin semiconductors”, *Nature Physics* **13**, 255–261 (2016).
- <sup>21</sup>D. K. Efimkin and A. H. MacDonald, “Many-body theory of trion absorption features in two-dimensional semiconductors”, *Physical Review B* **95** (2017) 10.1103/PhysRevB.95.035417.
- <sup>22</sup>R. Schmidt, T. Enss, V. Pietilä, and E. Demler, “Fermi polarons in two dimensions”, *Physical Review A* **85** (2012) 10.1103/PhysRevA.85.021602.
- <sup>23</sup>T. Kato and T. Kaneko, “Optical detection of a highly localized impurity state in monolayer tungsten disulfide”, *ACS Nano* **8**, 12777–12785 (2014).

## BIBLIOGRAPHY

- <sup>24</sup>S. Zhang, C.-G. Wang, M.-Y. Li, D. Huang, L.-J. Li, W. Ji, and S. Wu, “Defect structure of localized excitons in a WSe<sub>2</sub> monolayer”, *Physical Review Letters* **119** (2017) 10 . 1103 / PhysRevLett.119.046101.
- <sup>25</sup>J. Lindlau, C. Robert, V. Funk, J. Förste, M. Förg, L. Colombier, A. Neumann, E. Courtade, S. Shree, T. Taniguchi, K. Watanabe, M. M. Glazov, X. Marie, B. Urbaszek, and A. Högele, “Identifying optical signatures of momentum-dark excitons in transition metal dichalcogenide monolayers”, arXiv:1710.00988 [cond-mat] (2017).
- <sup>26</sup>C. Zhang, Y. Chen, A. Johnson, M.-Y. Li, L.-J. Li, P. C. Mende, R. M. Feenstra, and C.-K. Shih, “Probing critical point energies of transition metal dichalcogenides: surprising indirect gap of single layer WSe<sub>2</sub>”, *Nano Letters* **15**, 6494–6500 (2015).
- <sup>27</sup>W.-T. Hsu, L.-S. Lu, D. Wang, J.-K. Huang, M.-Y. Li, T.-R. Chang, Y.-C. Chou, Z.-Y. Juang, H.-T. Jeng, L.-J. Li, and W.-H. Chang, “Evidence of indirect gap in monolayer WSe<sub>2”</sub>, *Nature Communications* **8** (2017) 10 . 1038/s41467-017-01012-6.
- <sup>28</sup>M. Van der Donck, M. Zarenia, and F. M. Peeters, “Excitons, trions, and biexcitons in transition-metal dichalcogenides: magnetic-field dependence”, *Physical Review B* **97** (2018) 10 . 1103 / PhysRevB.97.195408.
- <sup>29</sup>A. Srivastava, M. Sidler, A. V. Allain, D. S. Lembke, A. Kis, and A. Imamoğlu, “Valley zeeman effect in elementary optical excitations of monolayer WSe<sub>2”</sub>, *Nature Physics* **11**, 141–147 (2015).
- <sup>30</sup>G. Aivazian, Z. Gong, A. M. Jones, R.-L. Chu, J. Yan, D. G. Mandrus, C. Zhang, D. Cobden, W. Yao, and X. Xu, “Magnetic control of valley pseudospin in monolayer WSe<sub>2”</sub>, *Nature Physics* **11**, 148–152 (2015).
- <sup>31</sup>D. V. Rybkovskiy, I. C. Gerber, and M. V. Durnev, “Atomically inspired  $k \cdot p$  approach and valley zeeman effect in transition metal dichalcogenide monolayers”, *Physical Review B* **95** (2017) 10 . 1103 / PhysRevB.95.155406.
- <sup>32</sup>N. Zibouche, P. Philipsen, A. Kuc, and T. Heine, “Transition-metal dichalcogenide bilayers: switching materials for spintronic and valleytronic applications”, *Physical Review B* **90**, 125440 (2014).
- <sup>33</sup>A. M. Jones, H. Yu, J. S. Ross, P. Klement, N. J. Ghimire, J. Yan, D. G. Mandrus, W. Yao, and X. Xu, “Spin-layer locking effects in optical orientation of exciton spin in bilayer WSe<sub>2”</sub>, *Nature Physics* **10**, 130–134 (2014).
- <sup>34</sup>V. Funk, “Spectroscopy of momentum-dark excitons in layered semiconductors” (LMU München, 2017).
- <sup>35</sup>J. Chen, W. Tang, B. Tian, B. Liu, X. Zhao, Y. Liu, T. Ren, W. Liu, D. Geng, H. Y. Jeong, H. S. Shin, W. Zhou, and K. P. Loh, “Chemical vapor deposition of high-quality large-sized MoS<sub>2</sub> crystals on silicon dioxide substrates”, *Advanced Science* **3**, 1500033 (2016).
- <sup>36</sup>A. K. Geim and K. S. Novoselov, “The rise of graphene”, *Nature Materials* **6**, 183–191 (2007).
- <sup>37</sup>F. Pizzocchero, L. Gammelgaard, B. S. Jessen, J. M. Caridad, L. Wang, J. Hone, P. Bøggild, and T. J. Booth, “The hot pick-up technique for batch assembly of van der waals heterostructures”, *Nature Communications* **7**, 11894 (2016).

## BIBLIOGRAPHY

- <sup>38</sup>W. Zhao, Z. Ghorannevis, K. K. Amara, J. R. Pang, M. Toh, X. Zhang, C. Kloc, P. H. Tan, and G. Eda, “Lattice dynamics in mono- and few-layer sheets of WS<sub>2</sub> and WSe<sub>2</sub>”, *Nanoscale* **5**, 9677 (2013).
- <sup>39</sup>X. Zhang, X.-F. Qiao, W. Shi, J.-B. Wu, D.-S. Jiang, and P.-H. Tan, “Phonon and raman scattering of two-dimensional transition metal dichalcogenides from monolayer, multilayer to bulk material”, *Chemical Society Reviews* **44**, 2757–2785 (2015).
- <sup>40</sup>P. Tonndorf, R. Schmidt, P. Böttger, X. Zhang, J. Börner, A. Liebig, M. Albrecht, C. Kloc, O. Gordán, D. R. T. Zahn, S. Michaelis de Vasconcellos, and R. Bratschitsch, “Photoluminescence emission and raman response of monolayer MoS<sub>2</sub>, MoSe<sub>2</sub>, and WSe<sub>2</sub>”, *Optics Express* **21**, 4908 (2013).
- <sup>41</sup>E. Courtade, B. Han, S. Nakhaie, C. Robert, X. Marie, P. Renucci, T. Taniguchi, K. Watanabe, L. Geelhaar, J. M. J. Lopes, and B. Urbaszek, “Spectrally narrow exciton luminescence from monolayer MoS<sub>2</sub> exfoliated onto epitaxially grown hexagonal BN”, arXiv:1804.06623 [cond-mat] (2018).
- <sup>42</sup>B. Arnaud, S. Lebègue, P. Rabiller, and M. Alouani, “Huge excitonic effects in layered hexagonal boron nitride”, *Physical Review Letters* **96** (2006) 10.1103/PhysRevLett.96.026402.
- <sup>43</sup>H. Li, J. Wu, X. Huang, Z. Yin, J. Liu, and H. Zhang, “A universal, rapid method for clean transfer of nanostructures onto various substrates”, *ACS Nano* **8**, 6563–6570 (2014).
- <sup>44</sup>A. Castellanos-Gomez, M. Buscema, R. Molenaar, V. Singh, L. Janssen, H. S. J. v. d. Zant, and G. A. Steele, “Deterministic transfer of two-dimensional materials by all-dry viscoelastic stamping”, *2D Materials* **1**, 011002 (2014).
- <sup>45</sup>D. H. Tien, J.-Y. Park, K. B. Kim, N. Lee, T. Choi, P. Kim, T. Taniguchi, K. Watanabe, and Y. Seo, “Study of graphene-based 2d-heterostructure device fabricated by all-dry transfer process”, *ACS Applied Materials & Interfaces* **8**, 3072–3078 (2016).
- <sup>46</sup>K.-H. Jung, D. G. Kim, and S.-B. Jung, “Adhesion of PDMS substrates assisted by plasma graft polymerization”, *Surface and Interface Analysis* **48**, 597–600 (2016).
- <sup>47</sup>Y.-C. Lin, C.-C. Lu, C.-H. Yeh, C. Jin, K. Suenaga, and P.-W. Chiu, “Graphene annealing: how clean can it be?”, *Nano Letters* **12**, 414–419 (2012).
- <sup>48</sup>N. Klein and H. Gafni, “The maximum dielectric strength of thin silicon oxide films”, *IEEE Transactions on Electron Devices* **ED-13**, 281–289 (1966).
- <sup>49</sup>A. L. Stancik and E. B. Brauns, “A simple asymmetric lineshape for fitting infrared absorption spectra”, *Vibrational Spectroscopy* **47**, 66–69 (2008).
- <sup>50</sup>U. Fano, “Effects of configuration interaction on intensities and phase shifts”, *Physical Review* **124**, 1866–1878 (1961).
- <sup>51</sup>G. Scuri, Y. Zhou, A. A. High, D. S. Wild, C. Shu, K. De Greve, L. A. Jauregui, T. Taniguchi, K. Watanabe, P. Kim, M. D. Lukin, and H. Park, “Large excitonic reflectivity of monolayer MoSe<sub>2</sub> encapsulated in hexagonal boron nitride”, *Physical Review Letters* **120** (2018) 10.1103/PhysRevLett.120.037402.
- <sup>52</sup>Y. Kang and S. Han, “An origin of unintentional doping in transition metal dichalcogenides: the role of hydrogen impurities”, *Nanoscale* **9**, 4265–4271 (2017).

## BIBLIOGRAPHY

- <sup>53</sup>K. Eshun, H. D. Xiong, S. Yu, and Q. Li, “Doping induces large variation in the electrical properties of MoS<sub>2</sub> monolayers”, *Solid-State Electronics* **106**, 44–49 (2015).
- <sup>54</sup>P. K. Chow, R. B. Jacobs-Gedrim, J. Gao, T.-M. Lu, B. Yu, H. Terrones, and N. Koratkar, “Defect-induced photoluminescence in monolayer semiconducting transition metal dichalcogenides”, *ACS Nano* **9**, 1520–1527 (2015).
- <sup>55</sup>Z. Lin, B. R. Carvalho, E. Kahn, R. Lv, R. Rao, H. Terrones, M. A. Pimenta, and M. Terrones, “Defect engineering of two-dimensional transition metal dichalcogenides”, *2D Materials* **3**, 022002 (2016).
- <sup>56</sup>G. Moody, C. Kavir Dass, K. Hao, C.-H. Chen, L.-J. Li, A. Singh, K. Tran, G. Clark, X. Xu, G. Berghäuser, E. Malic, A. Knorr, and X. Li, “Intrinsic homogeneous linewidth and broadening mechanisms of excitons in monolayer transition metal dichalcogenides”, *Nature Communications* **6** (2015) 10.1038/ncomms9315.
- <sup>57</sup>O. A. Ajayi, J. V. Ardelean, G. D. Shepard, J. Wang, A. Antony, T. Taniguchi, K. Watanabe, T. F. Heinz, S. Strauf, X.-Y. Zhu, and J. C. Hone, “Approaching the intrinsic photoluminescence linewidth in transition metal dichalcogenide monolayers”, *2D Materials* **4**, 031011 (2017).
- <sup>58</sup>C. R. Zhu, G. Wang, B. L. Liu, X. Marie, X. F. Qiao, X. Zhang, X. X. Wu, H. Fan, P. H. Tan, T. Amand, and B. Urbaszek, “Strain tuning of optical emission energy and polarization in monolayer and bilayer MoS<sub>2</sub>”, *Physical Review B* **88** (2013) 10.1103/PhysRevB.88.121301.
- <sup>59</sup>A. Srivastava, M. Sidler, A. V. Allain, D. S. Lembke, A. Kis, and A. Imamoğlu, “Optically active quantum dots in monolayer WSe<sub>2</sub>”, *Nature Nanotechnology* **10**, 491–496 (2015).
- <sup>60</sup>D. Vaclavkova, J. Wyzula, K. Nogajewski, M. Bartos, A. O. Slobodeniuk, C. Faugeras, M. Potemski, and M. R. Molas, “Singlet and triplet trions in WS<sub>2</sub> monolayer encapsulated in hexagonal boron nitride”, arXiv:1802.05538 [cond-mat] (2018).
- <sup>61</sup>G. Plechinger, P. Nagler, A. Arora, A. Granados del Águila, M. V. Ballottin, T. Frank, P. Steinleitner, M. Gmitra, J. Fabian, P. C. M. Christianen, R. Bratschitsch, C. Schüller, and T. Korn, “Excitonic valley effects in monolayer WS<sub>2</sub> under high magnetic fields”, *Nano Letters* **16**, 7899–7904 (2016).
- <sup>62</sup>A. V. Stier, K. M. McCreary, B. T. Jonker, J. Kono, and S. A. Crooker, “Exciton diamagnetic shifts and valley zeeman effects in monolayer WS<sub>2</sub> and MoS<sub>2</sub> to 65 tesla”, *Nature Communications* **7**, 10643 (2016).
- <sup>63</sup>A. A. Mitioglu, K. Galkowski, A. Surrente, L. Klopotowski, D. Dumcenco, A. Kis, D. K. Maude, and P. Plochocka, “Magnetoexcitons in large area CVD-grown monolayer MoS<sub>2</sub> and MoSe<sub>2</sub> on sapphire”, *Physical Review B* **93** (2016) 10.1103/PhysRevB.93.165412.
- <sup>64</sup>K. Hao, L. Xu, F. Wu, P. Nagler, K. Tran, X. Ma, C. Schüller, T. Korn, A. H. MacDonald, G. Moody, and X. Li, “Trion valley coherence in monolayer semiconductors”, *2D Materials* **4**, 025105 (2017).